A 1.3% distance to M33 from HST Cepheid photometry

Louise Breuval, Adam G Riess, Lucas M Macri, Siyang Li, Wenlong Yuan, Stefano Casertano, Tarini Konchady, Boris Trahin, Meredith J Durbin, Benjamin F Williams

The Astrophysical Journal, 951:118 (21pp), 2023 July 10 https://doi.org/10.3847/1538-4357/acd3f4

A 1.3% Distance to M33 from Hubble Space Telescope Cepheid Photometry

Louise Breuval[1], Adam G. Riess[1,2], Lucas M. Macri[3,4], Siyang Li[1], Wenlong Yuan[1], Stefano Casertano[2], Tarini Konchady[3], Boris Trahin[5], Meredith J. Durbin[6], and Benjamin F. Williams[6]
[1] Department of Physics and Astronomy, Johns Hopkins University, Baltimore, MD 21218, USA; lbreuva1@jhu.edu
[2] Space Telescope Science Institute, 3700 San Martin Drive, Baltimore, MD 21218, USA
[3] NSF's NOIRLab, 950 N Cherry Ave, Tucson AZ 85719, USA
[4] Department of Physics & Astronomy, Texas A&M University, College Station, TX 77843, USA
[5] Institut d'Astrophysique Spatiale, Université Paris-Saclay, CNRS, Batiment 121, F-91405 Orsay Cedex, France
[6] Department of Astronomy, University of Washington, Box 351580, U.W., Seattle, WA 98195-1580, USA
Received 2023 March 30; revised 2023 April 26; accepted 2023 May 8; published 2023 July 7

Abstract

We present a low-dispersion period–luminosity relation (PL) based on 154 Cepheids in Messier 33 (M33) with Hubble Space Telescope (HST) photometry from the PHATTER survey. Using high-quality ground-based light curves, we recover Cepheid phases and amplitudes for multi-epoch HST data and we perform template fitting to derive intensity-averaged mean magnitudes. HST observations in the SH0ES near-infrared Wesenheit system significantly reduce the effect of crowding relative to ground-based data, as seen in the final PL scatter of $\sigma = 0.11$ mag. We adopt the absolute calibration of the PL based on HST observations in the Large Magellanic Cloud and a distance derived using late-type detached eclipsing binaries to obtain a distance modulus for M33 of $\mu = 24.622 \pm 0.030$ mag ($d = 840 \pm 11$ kpc), a best-to-date precision of 1.3%. We find very good agreement with past Cepheid-based measurements. Several tip of the red giant branch estimates bracket our result while disagreeing with each other. Finally, we show that the flux contribution from star clusters hosting Cepheids in M33 does not impact the distance measurement and we find only ~3.7% of the sample is located in (or nearby) young clusters. M33 offers one of the best sites for the cross-calibration of many primary distance indicators. Thus, a precise independent geometric determination of its distance would provide a valuable new anchor to measure the Hubble constant.

Unified Astronomy Thesaurus concepts: Cepheid distance (217); Hubble constant (758); HST photometry (756); Galaxy distances (590)

Supporting material: machine-readable table

1. Introduction

Cepheid variables are the best-calibrated primary distance indicators and are commonly used to form the first rung of the empirical distance ladder (e.g., Riess et al. 2022). Their period–luminosity (PL) relation, also known as the "Leavitt Law" (Leavitt & Pickering 1912), is calibrated geometrically in the Milky Way from Gaia Data Release 3 parallaxes (Riess et al. 2021), in the Large Magellanic Cloud (LMC) from detached eclipsing binaries (DEBs) (Pietrzyński et al. 2019; Riess et al. 2019a), and in NGC 4258 with water masers (Reid et al. 2019). Cepheid distances are used to calibrate the second rung of the distance ladder, type Ia supernovae, which allows us to measure the distance to further galaxies in the Hubble flow and to derive the value of the Hubble constant, H_0.

Messier 33 (hereafter M33) is a nearby type Sc II-III spiral galaxy and the third largest member of the Local Group. As early as 1926, Edwin Hubble used this galaxy as one of the spiral nebulae to learn about the structure of the universe and observed 35 Cepheid variables to measure its distance (Hubble 1926). Since then, it has been extensively studied, and is still a crucial object for the distance scale (Freedman et al. 1991; Lee et al. 2022): M33 has intermediate inclination ($i = 57° \pm 4°$; Kourkchi et al. 2020),[7] which limits the effects of reddening and of geometry that can produce additional scatter in the PL relation. Additionally, M33 is known for its steep metallicity gradient, which was measured using red giant branch (RGB) stars (Tiede et al. 2004), planetary nebulae (Magrini et al. 2009), and H II regions (Bresolin 2011; Toribio San Cipriano et al. 2016; Rogers et al. 2022).

Cepheids are numerous in M33, and large samples have been obtained by various programs (Macri et al. 2001; Hartman et al. 2006; Pellerin & Macri 2011). Recently, the PHATTER collaboration (PI: J. Dalcanton) published a detailed catalog[8] of UV to near-infrared (NIR) photometry for 22 million stars in the central disk of M33 (Williams et al. 2021) using the Hubble Space Telescope (HST). Although they are not time-series observations, serendipitous overlaps between the PHATTER fields of view in a given filter provide multiple data points randomly spread across the phase of M33 Cepheids. Out of 250 Cepheids in the HST sample (defined in Section 2.2), 225 variables have more than one epoch in F475W and F814W, and 66 objects have more than one epoch in F160W (due to smaller overlaps of the WFC3/IR fields). Knowledge of the date and time of observation for each HST exposure, combined with periods previously measured from other surveys, enables the correction of these random-phase observations to mean magnitude. Finally, past studies (e.g., Macri et al. 2001; Riess et al. 2012; Wagner-Kaiser et al. 2015; Kodric et al. 2018) have revealed the advantages of space-based observations such as

[7] http://edd.ifa.hawaii.edu, Table "CF4 Initial Candidates."

[8] https://archive.stsci.edu/hlsp/phatter

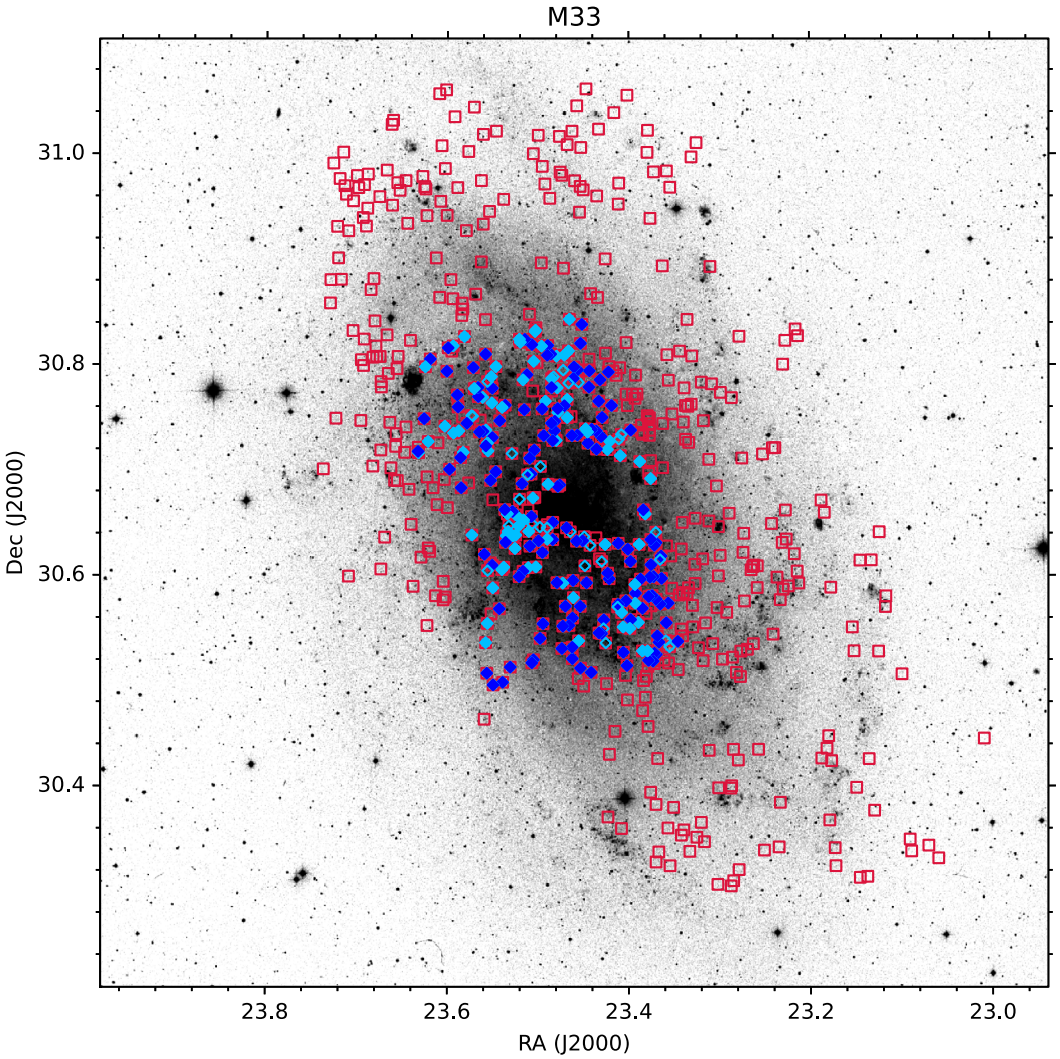

Figure 1. Map of M33: the template (i.e., ground-based) sample is shown in red, while the HST (i.e., PHATTER) sample is shown in blue. Dark blue and light blue markers are Cepheids from the gold and silver samples, respectively. Empty blue markers are excluded Cepheids (see Section 3.2). Note the HST sample is a subset of the template sample.

those by HST, in limiting crowding effects and their impact for the PL dispersion, as well as providing homogeneous photometry, including in the NIR. In this paper, we aim to take advantage of the recently published high-quality PHATTER catalog in order to provide a new PL calibration for M33 Cepheids in HST filters and to improve the M33 distance measurement.

The outline of this paper is the following. In Section 2 we present the samples of M33 Cepheids used in this study. In Section 3 we describe the construction of template light curves from ground-based data and the procedure to recover mean magnitudes from random-epoch photometry. In Section 4 we calibrate the Cepheid PL relation and determine the M33 distance modulus. Lastly, in Section 5 we investigate the effects of Cepheids located in star clusters, and we estimate their occurrence rate in M33 and compare it with that of other Local Group galaxies.

2. Photometric Data

In order to recover intensity-averaged mean magnitudes from random-phase HST data (hereafter the HST sample), we use templates obtained by compiling a large number of well-sampled ground-based light curves of M33 Cepheids (hereafter the template sample). Both samples are described below.

2.1. The Template Sample

We used a sample of 609 previously known Cepheids (Macri et al. 2001; Pellerin & Macri 2011) with homogeneous *gri* light curves obtained by T. Konchady et al. (2023, in preparation) using archival Canada–France–Hawaii Telescope (CFHT)/MegaCam observations (proposal ID 04BF26, PI: Beaulieu; proposal ID 04BH98, PI: Hodapp). They are represented in red in Figure 1 and constitute the template sample.

The majority of the original CFHT observations (associated with proposal ID 04BF26) are extensively described in Hartman et al. (2006); they span roughly 1.5 yr (2003 August to 2005 January) and were obtained on 27 separate nights. We supplemented these with an additional four nights of *i* observations obtained in 2004 August and September (associated with proposal ID 04HB98). T. Konchady et al. (2023, in preparation) performed an independent analysis of these images, carrying out time-series point spread function

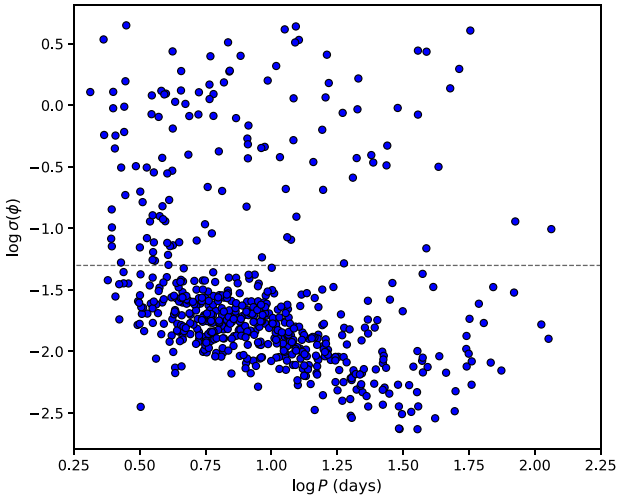

Figure 2. Distribution of phase uncertainties for Cepheids of the template sample at the epoch of HST observations, estimated from the period uncertainty and the interval between the midpoint of the HST and of the ground observations. The dashed horizontal line represents our threshold for the gold sample (see below): we only keep Cepheids with $\sigma(\phi) < 0.05$.

photometry that was calibrated against Pan-STARRS Data Release 1 (Chambers et al. 2016). The periods and phases of the Cepheids were redetermined by simultaneously fitting the CFHT *gri* photometry and the WIYN *BVI* photometry of Pellerin & Macri (2011) using the Yoachim et al. (2009) templates. We solved for a common period and phase across the six bands, and independent mean magnitudes and light-curve amplitudes in each band.

Cepheid light curves of the template sample have two purposes: they are used to build templates thanks to their complete phase coverage (see Section 3.1) and to recover the amplitudes and phases of the HST light curves (see Section 3.2). For this reason, their periods must be known precisely. From the period uncertainty, we estimate the uncertainty in the phase shift between the mid-date of the ground observations (MJD = 52,170) and of PHATTER observations (MJD = 57,989), and we flag Cepheids for which this uncertainty $\sigma(\phi)$ is larger than 0.05 (or $\log \sigma(\phi) > -1.3$, dashed horizontal line in Figure 2). They constitute the "silver" sample (see Section 3.2). Additionally, we only keep Cepheids that have optimal ground-based light curves (Table 3 of Pellerin & Macri 2011). This leaves a total of 420 Cepheids, for which we perform a visual inspection of each light curve's quality. Cepheids have an average of 45, 31, and 44 data points per light curve in *g*, *r*, and *i*, respectively.

We note that our ground-based sample is minimally affected by blending given the relatively high image quality of the CFHT and WIYN observations and the rejection of outliers by Pellerin & Macri (2011).

2.2. The Hubble Space Telescope Sample

The PHATTER survey (Williams et al. 2021) contains photometric measurements for 22 million stars in M33 with six UV to NIR filters (Advanced Camera for Surveys and Wide Field Camera 3) on the Hubble Space Telescope (HST). The survey focuses on the inner disk of the galaxy and covers $\sim$300 □′ (equivalent to a deprojected area of $\sim$38 kpc^2), extending up to $\sim$14′ from the center (equivalent to a distance of $\sim$3.5 kpc). The observations were taken between 2017 February 21 and 2018 February 25. The catalog reaches 26–28 mag in *V* depending on crowding. It is the largest and most complete catalog to date for stellar populations in M33. We identified 250 Cepheids from the template sample in the PHATTER catalog: they are represented in blue in Figure 1 and are hereafter referred to as the HST sample.

We matched the Cepheid coordinates to the full-frame PHATTER catalogs using an initial search radius of 0.″1, and found that all had matches within <0.5 mas with expected magnitudes ($19 < \mathrm{F475W} < 23$). We then used the pixel coordinates from these catalogs to retrieve the exposure-level photometry from the original DOLPHOT `.phot` outputs. These files contain columns with photometry from each individual input frame in addition to the combined measurements.

The PHATTER survey does not provide time-series observations, which might make it in principle poorly suited to study variable stars such as Cepheids. However, in the optical F475W and F814W filters, successive PHATTER pointings show significant overlap, and therefore up to four epochs can be available for a given Cepheid. In the NIR, the pointings have smaller overlaps, which gives one to two epochs per Cepheid. Each epoch can be decomposed into four or five separate dithers/exposures and the phase coverage of each epoch is random. We note that the first exposure of each F475W and F814W visit sequence is significantly shallower than the rest, as these are short exposures targeting the brightest stars (M. Durbin, 2023, private communication). They were therefore excluded as they are not useful for Cepheids. The date and time of a given HST observation provide the relative phase of the corresponding measurement. Then, mean magnitudes can be recovered from sparse data by applying a template-fitting procedure (Section 3).

3. Template Fitting

In this section, we describe the construction of template light curves from ground-based data (Section 3.1) and the procedure to recover mean magnitudes from PHATTER photometry in HST filters (Section 3.2). The HST and template samples were observed in different filters. The HST F475W filter is very similar to the *g* filter from CFHT/MegaCam, and F814W corresponds to the *i* filter (see Figure 3). Finally, the template sample does not cover the NIR up to the F160W filter; therefore, we use the Two Micron All Sky Survey (2MASS) *H*-band templates by Inno et al. (2015), based on a large sample of LMC Cepheid light curves. We adopt *g*-band and *i*-band templates to derive HST mean magnitudes in F475W and F814W, respectively, and *H*-band templates to derive F160W mean magnitudes.

3.1. Building Template Light Curves

We use the well-sampled light curves from the template sample to build template light curves in the *g*, *r*, and *i* filters of CFHT/MegaCam. These ground-based light curves are ideal to build templates and to recover the mean magnitudes from HST random-phase observations: they are representative of Cepheids from the HST sample as they belong to the same host galaxy and have a very similar period distribution (Figure 4). Other templates from the literature (e.g., Yoachim et al. 2009; from LMC Cepheids) could have been used instead of creating new ones. However, adopting templates built from a population similar to the HST sample avoids possible differences in

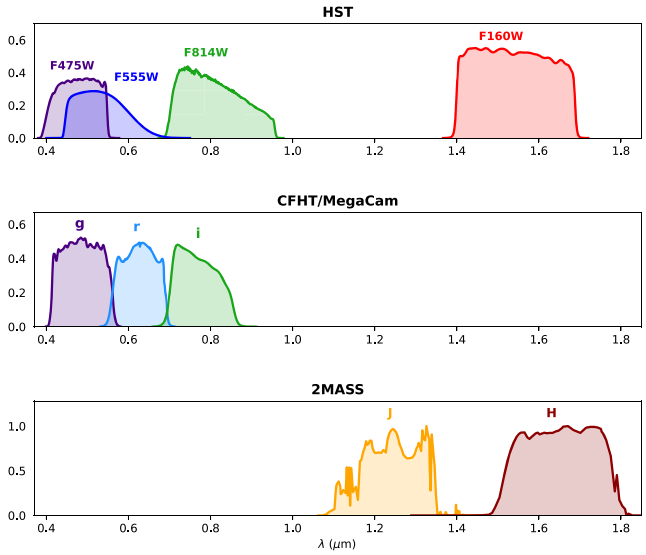

Figure 3. Wavelength coverage of HST filters used in this analysis (top panel), CFHT filters adopted to build optical template light curves (middle panel), and 2MASS filters used for NIR templates (Inno et al. 2015; bottom panel). We adopt g, i, and H templates to fit light curves in F475W, F814W, and F160W, respectively.

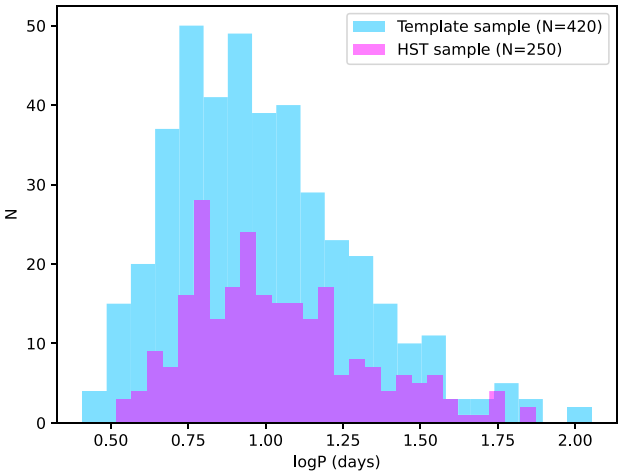

Figure 4. Period distribution of Cepheids from the template sample and from the HST sample.

light-curve shapes for Cepheids from different galaxies (possibly due to metallicity effects; Antonello et al. 2000).

In order to account for changes in light-curve shape as a function of period (Hertzsprung 1926), we split the sample into four different period bins. They are described in Table 1. The number of bins was determined by the size and by the distribution of our calibrating sample: having a larger sample would have allowed us to use more bins.

While the reference phase of a Cepheid is often defined by the epoch of maximum brightness, this quantity can be biased by the presence of a bump in the light curve that varies in shape and phase as a function of period along the Hertzsprung (1926) progression. This bump coincides with maximum light for Cepheids with periods of around 10 days. To overcome this issue, Inno et al. (2015) adopted another feature to determine the phase of a Cepheid light curve: the mean magnitude along the rising branch (MRB). As mean magnitudes are known with great precision for our template sample, this approach is more reliable than using the maximum to set the phase (see more details in Inno et al. 2015) and we adopt it in our analysis:

Table 1
Number of Cepheids in Each Period Bin for the Template Sample

Bin	$\log P$	N_g	N_r	N_i
1	0.3–0.9	148	136	143
2	0.9–1.2	91	84	81
3	1.2–1.5	46	47	44
4	1.5–2.0	20	19	16

$$\phi_{\rm obs} = \mathrm{mod}\left(\frac{\mathrm{JD_{obs}} - \mathrm{JD_{MRB}}}{P}\right). \quad (1)$$

For a filter λ, we normalize the magnitude values m_i by deriving the quantity

$$T_\lambda = \frac{m_i - \langle m_i \rangle}{A_\lambda}, \quad (2)$$

where $\langle m_i \rangle$ is the mean magnitude and A_λ is the amplitude. Finally, we merge all phased and normalized light curves into a single template for each period bin. The final templates and compiled light curves are shown in Figure 5 in the g, r, and i filters and for each of the four period bins. We follow Inno et al. (2015) and fit the merged light curves with a seventh-order Fourier series of the form

$$F_7(\phi) = A_0 + \sum_{i=1}^{7} A_i \cos(2\pi i\phi + \Phi_i). \quad (3)$$

The resulting coefficients are listed in Table 2.

3.2. Template Fitting Procedure

Before performing the fit, we set the first-guess V-band (F475W) amplitude A_V to that of the ground-based g-band light curve. Then, we fix the amplitude ratios to $A_I = 0.58\,A_V$ from Yoachim et al. (2009) and to

$$A_H = \begin{cases} 0.34\,A_V & \text{if } P \leqslant 20 \text{ days} \\ 0.40\,A_V & \text{if } P > 20 \text{ days} \end{cases}, \quad (4)$$

from Inno et al. (2015). The first-guess phase in F475W is set to the phase in g. By comparing CFHT g and i light curves, we derive a small phase lag between V and I of: $\phi_I = \phi_V + 0.027$, and we adopt the H-band phase lag from Inno et al. (2015) for F160W: $\phi_H = \phi_V + 0.080 - 0.002 \log P$. We note that Soszyński et al. (2005) derived a different phase lag of about 0.3 between H and V, but that is largely due to the choice of a different reference phase (maximum brightness). In Section 4.5 we discuss the sensitivity of our results to the phase lag.

We fit the templates to the HST measurements in the three filters simultaneously by performing a grid search on A_V and ϕ_V, where ϕ_V has a narrow, informative prior from the template sample. The amplitude ratios are fixed throughout the procedure and we retain as final parameters the solution that minimizes the quantity:

$$Z = \chi^2_{\rm tot} + Q(A_V), \quad (5)$$

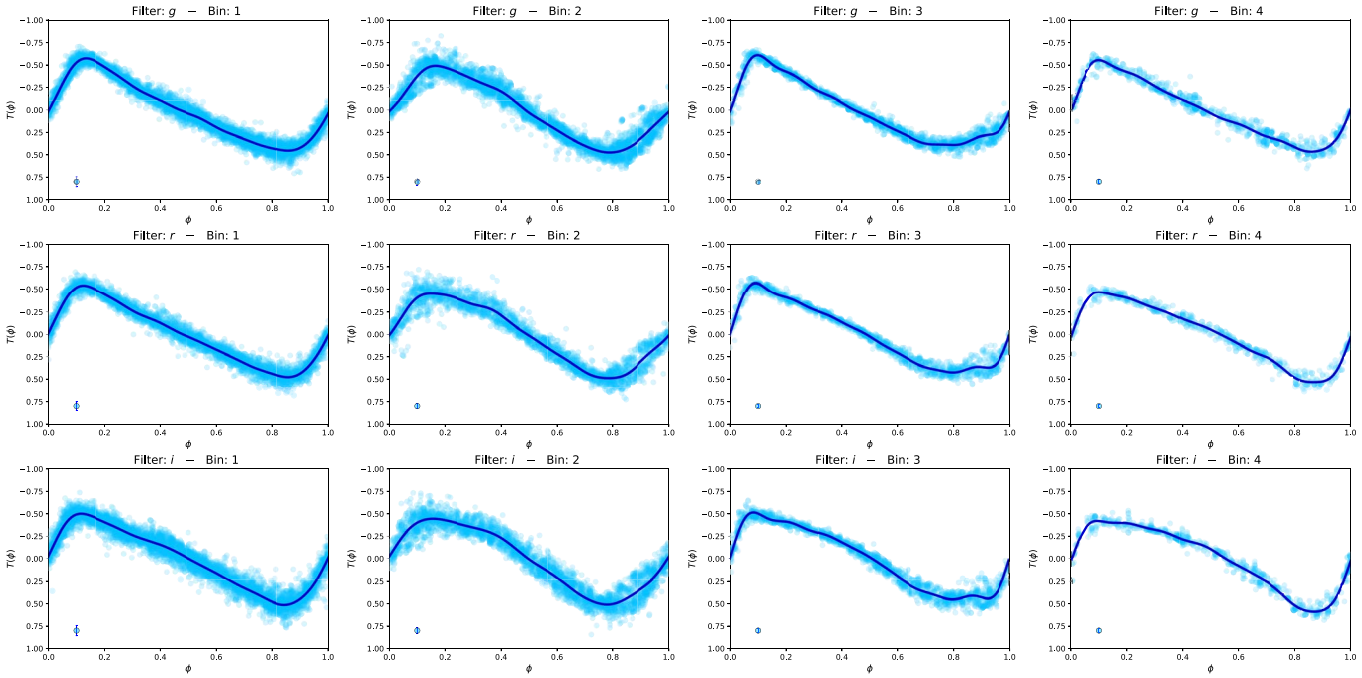

Figure 5. Merged light curves of M33 Cepheids (amplitude scaled) used for the templates in the *g*, *r*, and *i* band (first, second, and third lines, respectively). The four columns correspond to the four period bins listed in Table 1. The point in the bottom-left corner shows the typical error bar, multiplied by a factor of 3 for better visibility.

where $\chi^2_{\rm tot} = \chi^2_H + \chi^2_V + \chi^2_I$ and each χ^2 is defined as

$$\chi^2 = \sum_i \frac{(O_i - C_i)^2}{\sigma_i^2}, \quad (6)$$

with O_i the data points, C_i the fit values, and σ_i the error of each data point. The quantity $Q(A_V)$ is a penalty function that prevents the fitted HST amplitudes to diverge too far from the expected values (i.e., the *g*-band amplitude of each Cepheid). It is defined as

$$Q(A_V) = \frac{(A_{V,\rm fitted} - A_{V,\rm ground})^2}{\sigma_A^2}. \quad (7)$$

The dispersion in the difference in amplitudes is set to $\sigma_A = 0.030$ mag from the ground-based sample. Finally, the errors on each apparent magnitude are estimated from a χ^2 distribution assuming $\chi^2 < \chi^2_{\rm min} + 1$ (Press et al. 1992). Figure 6 shows a few examples of light curves obtained from the template fitting procedure.

In the following, we consider two different subsamples. The gold sample includes Cepheids for which the phase is known with good confidence from ground-based light curves: these Cepheids have at least a valid *g*-band light curve or a valid *i*-band light curve (or both ideally). In the case where only one light curve is available among *g* and *i*, amplitudes and phases in the missing band can be easily recovered from the relations adopted above. Cepheids of the gold sample must also have a phase uncertainty of $\sigma_\phi < 0.05$ to allow for a precise rephasing of HST observations. As their phase and amplitude are assumed to be known from the ground, the grid search is performed on a limited range of parameters: across $[A_V - 0.4; A_V + 0.4]$ in amplitude and $[\phi_V - 0.05; \phi_V + 0.05]$ in phase. The silver sample includes Cepheids with no *g* and no *i* light curves or with a larger phase uncertainty $\sigma_\phi > 0.05$. For these stars, the phasing is considered unknown and we perform the grid search over [0; 1] in phase. The expected amplitude of these silver sample Cepheids is also unknown: as the mean *V*-band peak-to-peak amplitude of our sample is 0.8 mag, we perform the grid search within [0.3, 1.3] in amplitude, which corresponds to 0.8 ± 0.5 mag. After a visual inspection of each light curve, we find nine Cepheids from the gold sample that appear to have an incorrect phasing (i.e., reaching the boundaries of the grid search in ϕ_V): for these stars we allow the search to cover [0; 1] in phase (but generally the final phase stays within ± 0.1 from the first guess) and we find much lower χ^2 and better fit quality. These nine stars are moved to the silver sample.

Out of the 250 initial PHATTER Cepheids, we only keep the 220 that have optimal ground-based light curves (Table 3 from Pellerin & Macri 2011). We rejected 29 stars with only one epoch per filter or with multiple but very close epochs ($\Delta\phi < 0.01$), which did not allow the fit to converge successfully. We also excluded 26 stars for which the fit was not satisfactory and 11 stars that yielded a fitted *V*-band amplitude different by more than 0.5 mag from the expected amplitude from ground-based light curves. This leaves a total of 154 Cepheids that constitute the "gold+silver" sample. The final intensity-averaged mean magnitudes obtained for our sample of Cepheids in F160W, F475W, and F814W are listed in Table 9 (Appendix A).

4. Period–Luminosity Relation and Distance to M33

4.1. Photometric Transformations to WFC3

In order to derive the distance to M33, we will compare its PL relation with that established in the LMC, which has the most precise and Cepheid-independent distance measurement (Pietrzyński et al. 2019). The LMC PL relation (Riess et al. 2019a) is calibrated in the SH0ES photometric system based on

Table 2
Fourier Parameters for Template Light Curves Obtained with the Calibrating Sample of Cepheids

Bin	A_0	A_1	A_2	A_3	A_4	A_5	A_6	A_7	Φ_1	Φ_2	Φ_3	Φ_4	Φ_5	Φ_6	Φ_7
								g							
1	0.004	0.431	0.161	0.062	0.022	0.007	0.004	−0.005	1.665	1.502	1.132	0.918	0.043	0.036	1.649
2	0.007	0.450	−0.073	0.019	0.020	0.008	0.005	−0.004	1.615	−1.554	0.747	−0.567	-1.423	−13.477	1.027
3	0.004	0.424	0.134	0.074	0.052	0.032	0.025	0.014	1.802	1.615	1.113	0.924	0.714	0.511	0.289
4	−0.001	0.415	0.169	0.082	−0.040	−0.023	0.014	0.008	1.656	1.587	1.555	−1.682	−1.854	0.464	0.749
								r							
1	0.003	0.429	−0.162	0.064	0.023	−0.007	0.005	−0.005	1.642	−7.820	1.409	1.078	3.979	−0.036	−4.029
2	0.005	0.451	−0.076	0.019	0.022	0.009	0.007	0.008	1.616	−1.273	1.251	0.046	−0.583	−0.073	−0.397
3	0.002	0.431	−0.135	0.081	0.057	0.039	0.024	0.013	1.694	−1.447	1.322	1.181	1.090	1.003	0.952
4	−0.001	0.422	−0.173	−0.082	−0.037	0.022	−0.017	−0.009	1.477	4.767	−7.740	−7.727	1.217	−1.784	−1.636
								i							
1	0.005	0.429	−0.156	−0.065	0.019	0.008	0.008	−0.003	1.595	−1.378	−1.505	1.399	1.025	0.346	−2.680
2	0.007	0.462	−0.080	0.024	0.022	0.005	−0.005	0.002	1.599	−1.124	1.579	0.527	−4.821	16.604	14.585
3	0.004	0.448	−0.131	0.082	0.058	0.039	0.029	0.012	1.601	−1.400	1.422	1.424	1.365	1.382	−11.207
4	−0.002	0.440	−0.171	−0.082	−0.037	0.023	−0.015	0.010	1.382	−1.433	−1.285	−1.166	1.450	−1.479	1.365

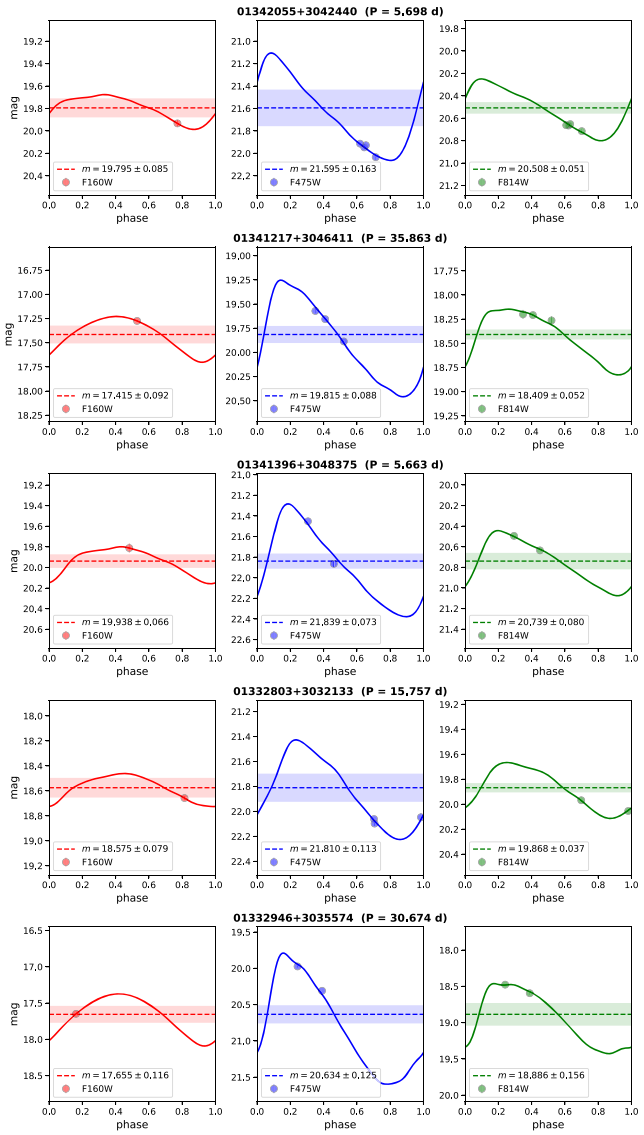

Figure 6. Example of light curves obtained from the template fitting procedure. Their quality is representative of that of the entire sample. The shaded area represents the mean magnitude error in each filter. For a given star, the three filters are shown with the same scale in magnitude.

HST/WFC3 filters (F160W, F555W, and F814W). On the other hand, the mean magnitudes obtained in the present work from PHATTER photometry were measured with the WFC3/IR camera for the F160W filter and with ACS/WFC for the optical F475W and F814W filters. We transform the PHATTER color $(\mathrm{F475W}-\mathrm{F814W})_{\mathrm{ACS}}$ into the SH0ES color $(\mathrm{F555W}-\mathrm{F814W})_{\mathrm{WFC3}}$ using synthetic populations based on PARSEC isochrones generated by the color–magnitude diagram tool[9] developed by Bressan et al. (2012) (version v3.7) for HST/WFC3 and HST/ACS bandpasses. We consider a population of Cepheid-like stars with ages of 1–500 Myr, $\log g < 2$, masses of 3–7 $M_{\odot}$, and temperatures of 4800–6500 K. The theoretical isochrones are derived assuming an extinction of $A_V = 0.2$ mag, which corresponds to the foreground extinction in the direction of M33 (Schlafly & Finkbeiner 2011). We derive the following transformation with a scatter of 0.003 mag:

$$(\mathrm{F555W}-\mathrm{F814W})_{\mathrm{WFC3}} = 0.065 + 0.658\,(\mathrm{F475W}-\mathrm{F814W})_{\mathrm{ACS}}. \quad (8)$$

The mean Cepheid color of the sample is $(\mathrm{F475W}-\mathrm{F814W})_{\mathrm{ACS}} = 1.41$ mag (sample standard deviation = 0.29 mag), for which Equation (8) gives $(\mathrm{F555W}-\mathrm{F814W})_{\mathrm{WFC3}} = 0.99$ mag (sample standard deviation = 0.19 mag). In the following, we adopt the NIR HST/WFC3 Wesenheit index defined in Riess et al. (2022), assuming the reddening law from Fitzpatrick (1999) with reddening parameter $R_V = 3.3$:

$$m_H^W = \mathrm{F160W} - 0.386\,(\mathrm{F555W}-\mathrm{F814W})_{\mathrm{WFC3}}. \quad (9)$$

We also derive optical Wesenheit magnitudes defined in Riess et al. (2019a) as

$$m_I^W = \mathrm{F814W} - 1.3\,(\mathrm{F555W}-\mathrm{F814W})_{\mathrm{WFC3}}. \quad (10)$$

4.2. Count-rate Nonlinearity Correction

The WFC3-IR instrument, which is used in the SH0ES distance ladder to measure nearby bright Cepheids as well as distant stars in supernovae host galaxies, is affected by count-rate nonlinearity (CRNL, or reciprocity failure). This effect dims faint sources relative to bright ones due to a decreased photon collection efficiency. Its most recent calibration gives a correction of 0.0077 mag dex^{-1} (Riess et al. 2019b). In order to derive the distance to M33, m_H^W magnitudes in the LMC and in M33 must be corrected for the CRNL consistently. The PL intercept of 15.898 mag calibrated in the LMC by Riess et al. (2019a) does not include the CRNL term (despite its note to the contrary, see footnote to Table 5 of Yuan et al. 2020). Finally, M33 Cepheids are fainter than LMC Cepheids by about 2 dex (Li et al. 2021), so we add 0.015 ± 0.005 mag to the LMC intercept from Riess et al. (2019a) to account for this difference (which is equivalent to subtracting 0.015 mag to our m_H^W apparent magnitudes in M33).

4.3. Geometric Correction

We take into account the position of each Cepheid relative to the center of M33 ($\alpha = 23.4625°$, $\delta = 30.6602°$ from van der Marel et al. 2019) by applying a geometric correction. Our HST sample is located very near the center of M33 and the galaxy has a moderate inclination, which limits the effects of projection and of reddening. We adopt an inclination angle of $i = 57° \pm 4°$ and a position angle of PA $= 22.5°$ (both from Kourkchi et al. 2020), obtaining a mean correction of 0.0007 mag with a dispersion of 0.003 mag, with values ranging between -0.005 and $+0.008$ mag. A positive geometric correction corresponds to a Cepheid farther than the center of M33.

4.4. Period–Luminosity Relation in M33

In this section, we adopt the apparent Wesenheit m_H^W mean magnitudes obtained from template fitting for our sample of M33 Cepheids. We include an additional 0.07 mag in quadrature to all magnitude errors to account for the finite width of the instability strip (Riess et al. 2019a). The PL relation is then calibrated for the two subsamples defined in Section 3 (gold and silver samples).

[9] http://stev.oapd.inaf.it/cgi-bin/cmd

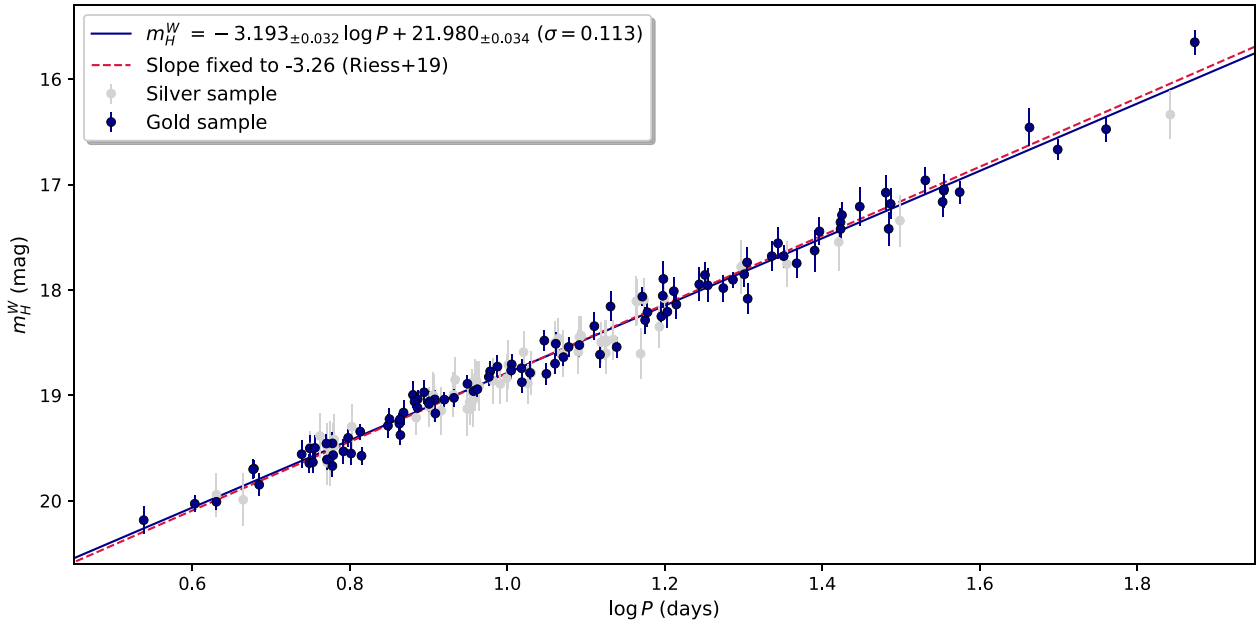

Figure 7. Period–luminosity relation in m_H^W for M33 Cepheids. The dark solid line is the PL fit of the gold + silver sample assuming a free slope, and the red dashed line shows the same fit when the slope is fixed to -3.26 mag dex^{-1} (Riess et al. 2019a).

Table 3
Calibration of the PL Relation in M33 ($m = \alpha \log P + \beta$) and Resulting Distance Modulus

Band	α	$\beta_{\rm free}$	$\beta_{\rm fixed}$	σ	$\chi^2_{\rm dof}$	$N_{\rm stars}$	Sample	$\mu_{\rm M33}$ (mag)
m_H^W	-3.207 ± 0.039	21.993 ± 0.041	22.046 ± 0.010	0.110	0.96	99	Gold	24.619 ± 0.030
m_H^W	-3.193 ± 0.032	21.980 ± 0.034	22.048 ± 0.008	0.113	0.72	154	Gold + Silver	**24.622 ± 0.030**
m_I^W	-3.167 ± 0.046	21.909 ± 0.051	22.065 ± 0.014	0.141	1.32	99	Gold	24.617 ± 0.032
m_I^W	-3.179 ± 0.037	21.933 ± 0.041	22.072 ± 0.010	0.130	1.01	154	Gold + Silver	24.624 ± 0.030

Notes. The second column gives the fitted PL slope α. The third and fourth columns give the PL intercept β when the slope is a free parameter and when the slope is fixed to the LMC value (Riess et al. 2019a), respectively. The bold value shows the final adopted distance and uncertainty.

For the gold sample we obtain a slope of -3.207 ± 0.039 mag dex^{-1} in m_H^W, which agrees well with that derived by Riess et al. (2019a) in the LMC. The PL scatter is 0.110 mag for a total of 99 stars. Including the silver sample yields a slightly shallower slope of -3.193 ± 0.032 mag dex^{-1}, which is still in good agreement with Riess et al. (2019a), and slightly raises the scatter to 0.113 mag. In the optical Wesenheit index m_I^W, we adopt the slope of -3.31 mag dex^{-1} as well as the LMC PL intercept of 15.935 from Riess et al. (2019a) and we obtain a PL dispersion of 0.13 mag for the gold + silver sample, and 0.14 for the gold sample. We note that Li et al. (2021) obtained a PL scatter of 0.13 mag in M31 for their gold sample with 42 Cepheids, which shows the great precision of our PL calibration. Our PL coefficients are listed in Table 3 and the PL relation is shown in Figure 7.

4.5. Distance to M33

To obtain the distance modulus for M33 ($\mu_{\rm M33}$), we compare the intercept of our m_H^W PL relation in M33 with that of the LMC obtained by Riess et al. (2019a), $m_H^W = 15.898 - 3.26 \log P$. We add the CRNL term of 0.015 mag to the LMC intercept to account for the difference in brightness between LMC and M33 Cepheids (see Section 4.2). We fix our PL slope to -3.26 for consistency with the LMC and we derive

$$(\mu_{\rm M33} - \mu_{\rm LMC}) = (\beta_{\rm M33} - \beta_{\rm LMC}) + \Delta m, \quad (11)$$

where $\mu_{\rm LMC} = 18.477 \pm 0.026$ mag is the most direct and precise geometric distance to the LMC available (Pietrzyński et al. 2019). The term Δm is the correction for the difference in metallicity between M33 and LMC Cepheids:

$$\Delta m = -\gamma\ ([{\rm O/H}]_{\rm M33} - [{\rm O/H}]_{\rm LMC}) \quad (12)$$

Romaniello et al. (2022) give $[{\rm O/H}]_{\rm LMC} = -0.32 \pm 0.01$ dex from a sample of 89 Cepheids. In M33 we use the metallicity gradient by Bresolin (2011), which gives

$$12 + \log({\rm O/H}) = 8.50_{\pm 0.02} - 0.045_{\pm 0.006}\ R_{\rm kpc}, \quad (13)$$

relative to 8.69 for solar (Asplund et al. 2009), where $R_{\rm kpc}$ is the deprojected galactocentric distance derived using the parameters given in Section 4.3 (coordinates of the center, PA, and inclination). For our HST sample, [O/H] metallicities range from -0.20 dex to -0.36 dex. We adopt the mean metallicity of $[{\rm O/H}]_{\rm M33} = -0.27 \pm 0.03$ dex. Using the metallicity correction of $\gamma = -0.217 \pm 0.046$ mag dex^{-1} from Riess et al. (2022), we obtain a correction of $\Delta m = 0.011 \pm 0.007$ mag. Using the metallicity correction from Breuval et al. (2022) returns

Table 4
Error Budget for the Distance to M33

Error	Value	Source
LMC DEBs	1.20%	Pietrzyński et al. (2019)
LMC PLR mean	0.41%	Riess et al. (2019a)
M33 PLR mean	0.38%	Measured here
Metallicity correction	0.33%	Riess et al. (2022)
CRNL across 2 dex	0.23%	Riess et al. (2019b)
Total	1.38%	

$\Delta m = 0.014$ mag, which is very similar, but we adopt the former as it is more suited for measurements in the Wesenheit m_H^W index. From Equation (11) we obtain a final distance modulus of 24.622 ± 0.030 mag based on the gold and silver samples combined in the NIR Wesenheit index m_H^W. Using only the pure gold sample results in a very similar value (see Table 3). Finally, the optical Wesenheit index yields a very consistent distance of 24.617 ± 0.032 and 24.624 ± 0.030 mag from the gold sample only and gold + silver samples combined, respectively. We retain as the final distance modulus the one from the gold + silver sample in the m_H^W filter, 24.622 ± 0.030 mag, as it is based on the most precise PL intercept. The full error budget is detailed in Table 4.

In Section 3.2, we adopted the phase lag from Inno et al. (2015) between H and V light curves ($\sim$0.08, with a scatter of 0.03 in the relation), derived by using the mean magnitude along the rising branch as a reference for the phase. We made this choice for consistency, as we also use the NIR templates by Inno et al. (2015). On the other hand, Soszyński et al. (2005) found a larger phase lag of $\sim$0.3 (with a larger scatter of about 0.1 mag) by using the phase at maximum brightness as a reference. Inno et al. (2015) show that these two methods to phase the data are very different; using the Soszyński et al. (2005) phase lag with the Inno et al. (2015) template is formally inconsistent, but it leads to a difference of only 0.006 mag in the distance modulus.

We attempted to independently constrain the value of the metallicity effect of the PL relation, γ. However, the very narrow range of abundances spanned by these Cepheids yields uncertainties $\sigma(\gamma)$ of 0.24–0.42 mag dex^{-1}, which do not improve upon previous measurements (Breuval et al. 2021, 2022; Riess et al. 2022).

4.6. Comparison with the Literature

4.6.1. Cepheids, RR Lyrae, and Miras

Figure 8 shows our final distance modulus for M33 and compares it with other values from the literature based on various indicators (listed in Table 5), all corrected to a common LMC distance modulus of 18.477 mag (Pietrzyński et al. 2019). Our distance agrees very well with other estimates based on Cepheids, especially with Freedman et al. (1991), Macri (2001), Scowcroft et al. (2009), and Bhardwaj et al. (2016). In particular, Cepheids appear to provide the most consistent distance measurements among all other distance indicators. The error of the Pellerin & Macri (2011) distance was revised to 0.05 mag to include the systematic uncertainties from the photometric comparison with Massey et al. (2006) in their Section 3. The Cepheid distance to M33 by Lee et al. (2022) is larger than our value by 0.10 mag (1.7σ). This difference matches the size and direction of the metallicity dependence of Cepheids, ~ -0.2 mag dex^{-1} (Breuval et al. 2022), where metal-poor Cepheids are fainter. (It is the wrong direction for crowding, which, if uncorrected, would make ground-based observations of Cepheids appear too bright.) The Lee et al. (2022) sample is in the outer regions of M33, around 5 kpc from the center, which corresponds to a metallicity of about [O/H] ~ -0.4 dex, somewhat metal-poor. They derive their distance to M33 relative to the absolute PL calibration by Monson et al. (2012), based on Milky Way Cepheids, which are metal-rich with [O/H] ~ 0.1 dex. This 0.5 dex difference in metallicity produces an expected difference of $\sim$0.10 mag, bringing it into agreement with the study here. An alternative to correcting for metallicity is to use a reference with a similar metallicity as M33, i.e., the metal-poor Cepheids in the LMC, ~ -0.3 dex, and the geometric DEB distance as a reference for the Lee et al. (2022) sample, which we find yields 24.65 mag and is in good agreement with our result. We also find good agreement with the RR Lyrae distance by Sarajedini et al. (2006). Finally, the two Mira-based distances (Yuan et al. 2018; Ou et al. 2023) differ by 0.13 mag, which can be attributed to the use of different data sets and methodologies and differences in periods and possible calibration systematics between ground- and space-based data.

4.6.2. Tip of the Red Giant Branch

Distance moduli based on the tip of the red giant branch (TRGB) show a larger dispersion than Cepheid-based measurements with differences as large as 0.34 mag between different studies. For example, McConnachie et al. (2004) derive a distance modulus of 24.50 ± 0.06 mag based on an annulus region between 0.5° and 0.8° in the outer disk of M33. They investigate the impact of crowding and conclude that this effect is negligible in regions farther than 0.5° from the center of M33. They also rule out the possibility of contamination from asymptotic giant branch (AGB) stars. More recently, Lee et al. (2022) selected a TRGB field in the southern part of M33 at a distance of about 0.25°–0.45° from the galactic center, and therefore no less likely to be affected by blending than the McConnachie et al. (2004) sample, yet obtained a much higher distance modulus of 24.72 ± 0.06 mag. We speculate some of this difference could be attributed, in part, to a difference in sample color, as the redder color cut from Lee et al. (2022) extends further into the region where the TRGB is fainter and may benefit from a color correction (see Jang & Lee 2017). We note that although the mean color of the sample from Lee et al. (2022) is located at the boundary where Jang & Lee (2017) state a color correction is not necessary, Jang & Lee (2017) do not calibrate their color relation based on the mean color of their entire sample. It is also possible the different TRGB-based measurements are due to population differences, as recently seen in Hoyt (2023), Anderson et al. (2023), and Wu et al. (2022), which all identify significant, intrinsic variations in the TRGB brightness with location, sub-RGB population, or the apparent ratio of RGB to AGB stars (that may relate to age or metallicity). Durbin et al. (2020) also identify additional systematics associated with the TRGB by comparing different calibration approaches. The χ^2 of the TRGB measurements around their weighted mean value is 3.67, compared to 1.42 for Cepheid-based distances (see

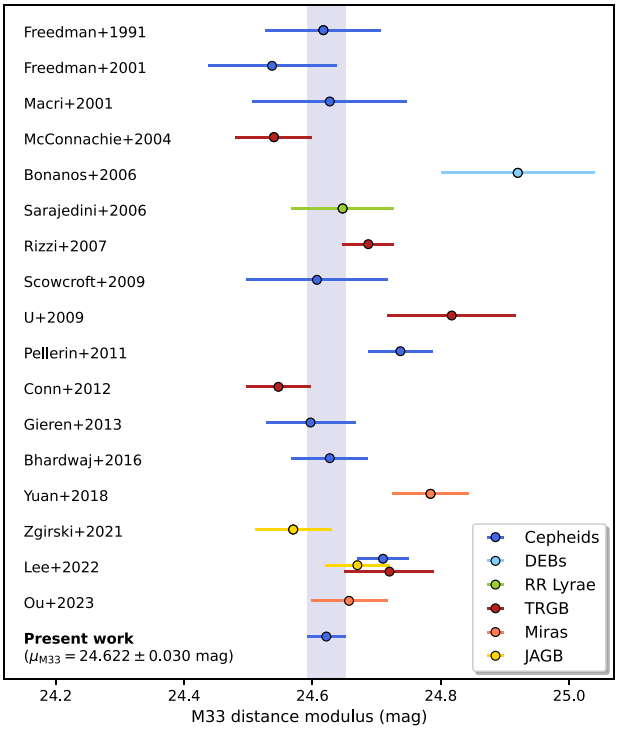

Figure 8. M33 distance modulus from the present work compared with values from the literature. All values shown here are rescaled to the recent LMC distance modulus of 18.477 from Pietrzyński et al. (2019; see their original adopted LMC distance in Table 5).

Table 5
M33 Distance Modulus from the Literature

μ_{M33}	References	Method	μ_{LMC}
24.64 ± 0.09	Freedman et al. (1991)	Cepheids	18.50
24.56 ± 0.10	Freedman et al. (2001)	Cepheids	18.50
24.65 ± 0.12	Macri (2001)	Cepheids	18.50
24.54 ± 0.06	McConnachie et al. (2005)	TRGB	···
24.92 ± 0.12	Bonanos et al. (2006)(*)	DEBs	···
24.67 ± 0.08	Sarajedini et al. (2006)	RR Lyrae	18.50
24.71 ± 0.04	Rizzi et al. (2007)	TRGB	···
24.53 ± 0.11	Scowcroft et al. (2009)	Cepheids	18.40
24.84 ± 0.10	U et al. (2009)	TRGB	18.50
24.76 ± 0.05	Pellerin & Macri (2011)	Cepheids	18.50
24.57 ± 0.05	Conn et al. (2012)	TRGB	···
24.62 ± 0.07	Gieren et al. (2013)	Cepheids	18.50
24.62 ± 0.06	Bhardwaj et al. (2016)	Cepheids	18.47
24.80 ± 0.06	Yuan et al. (2018)	Miras	18.493
24.57 ± 0.06	Zgirski et al. (2021)	JAGB	18.477
24.67 ± 0.05	Lee et al. (2022)	JAGB	···
24.72 ± 0.07	Lee et al. (2022)	TRGB	···
24.71 ± 0.04	Lee et al. (2022)	Cepheids	···
24.67 ± 0.06	Ou et al. (2023)	Miras	18.49
24.622 ± 0.030	Present work	Cepheids	18.477

Notes. The last column gives the LMC distance modulus adopted to obtain the distances given in the first column. (*) The distance by Bonanos et al. (2006) is not fully empirical, contrary to all other distances listed here, and relies on surface flux calculated from non-local thermodynamic equilibrium models (see Section 4.6.3).

Table 6). Finally, both measurements based on the JAGB method (Zgirski et al. 2021; Lee et al. 2022) agree to 1σ with our value.

Table 6
Statistics of the M33 Distances from the Literature Based on Various Distance Indicators

Indicator (1)	Mean μ_{M33} (2)	$\chi^2_{mean,\nu}$ (3)	$\chi^2_{B23,\nu}$ (4)	N (5)
Cepheids	24.644	1.08	1.39	9
TRGB	24.639	3.67	2.96	5
JAGB	24.625	1.65	0.84	2
Miras	24.721	2.24	3.84	2

Note. Column (2) is the weighted mean distance modulus for each indicator. Columns (3) and (4), respectively, give the χ^2 of the measurements from the literature around the weighted mean distance modulus and around the distance modulus of the present paper. Column (5) gives the number of estimates from the literature considered for each distance indicator.

4.6.3. Eclipsing Binaries

A distance to M33 based on DEBs was published by Bonanos et al. (2006). However, unlike the well-established LMC and distances by Pietrzyński et al. (2019) and Graczyk et al. (2020), respectively, which are based on late-type DEBs (a purely empirical method calibrated geometrically through red giant interferometry), the M33 distance by Bonanos et al. (2006) relies on early-type DEBs, which depend on surface flux calculated from non-local thermodynamic equilibrium models and are strongly affected by model uncertainties. Therefore, we will not compare our result with this measurement as we limit our comparisons to empirical measures.

In the future, the ability to measure many primary distance indicators in the same host offers the best chance to identify and rectify differences between distance indicators. M33 offers one of the best such opportunities.

5. Photometric Bias from Cluster Cepheids

5.1. Motivation

Contamination from crowded backgrounds, such as star clusters, can bias photometric measurements of Cepheids in nearby galaxies. Photometric measurements of extragalactic Cepheids are usually corrected for crowding effects by injecting artificial stars in the vicinity of Cepheids and by remeasuring their contribution (Riess et al. 2009). However, this test may not properly reproduce the impact of stars physically associated with Cepheids, which might be unresolved and whose light properties might differ from those of the background field stars. Anderson & Riess (2018) found that blending due to cluster Cepheids was responsible for a 0.23% overestimate of H_0, although cluster Cepheids are a relatively rare phenomenon. They concluded that chance superposition of Cepheids with clusters was not a limit for a 1% measurement of the Hubble constant. In this section, we estimate the blending contribution from cluster Cepheids in M33: we measure the occurrence rate of Cepheids in clusters in M33 and we derive the typical flux contribution of the clusters in order to determine by how much they affect Cepheid photometry and our M33 distance modulus.

5.2. Crossmatch of Cepheid and Cluster Catalogs

First, we estimate the number of M33 Cepheids located in or near clusters. Anderson & Riess (2018) reported a fraction of 2.4% cluster Cepheids in the M31 galaxy, lower than in the

Table 7
Cluster Cepheids Found by Crossmatching Cepheids from Pellerin & Macri (2011) and Star Clusters from Johnson et al. (2022) with $\theta_{sep} < 1.2\ r_{ap}$, where r_{ap} Is the Average Cluster Radius

Cepheid	Cluster	r_{ap} ($''$)	θ_{sep} ($''$)
01334331+3043559	J22-241	1.17	0.85
01340959+3036215	J22-477	1.55	1.46
01340060+3050079	J22-521	1.83	1.77
01332060+3034584	J22-665	1.49	0.12
01342512+3034381	J22-722	1.41	0.27
01335311+3048343	J22-836	1.43	0.49
01335809+3045568	J22-900	1.31	1.51
01332768+3034238	J22-1464	1.32	0.26
01334212+3032109	J22-1492	1.60	1.74
01342784+3041012	J22-1762	1.35	1.04

Milky Way, LMC, and SMC (with 8.5%, 11%, and 6%, respectively). In order to obtain the fraction of cluster Cepheids in M33, we crossmatch an initial sample of 609 fundamental-mode Cepheids from Pellerin & Macri (2011) with the catalog of 2137 star clusters in M33 from Johnson et al. (2022). We adopt a separation of $\theta_{sep} < 1.2\ r_{ap}$ as membership criteria (Senchyna et al. 2015), with r_{ap} the mean cluster radius provided in Johnson et al. (2022). From this crossmatch we find a total of 10 cluster Cepheids, listed in Table 7.

5.3. Creation of Stamp Images

We identified these 10 cluster Cepheids in the PHATTER mosaics and we produced stamp images (cutouts centered on each Cepheid) in each filter. The HST stamp images of the 10 crossmatched cluster Cepheids are shown in Figure 11 (Appendix B), where the clusters are easy to identify by eye. In particular, UV filters (F275W and F336W) are well suited for detecting hot blue cluster stars, while background red giant stars with luminosity similar to that of the Cepheid may contribute more in the infrared. We note that some stamps are blank because the Cepheid is located outside the limit of the PHATTER fields in NIR and UV.

5.4. Visual Inspection of Stamp Images

In order to make sure that the cluster count is complete, we inspected each Cepheid stamp image for the presence of any additional undetected clusters. We report an additional 13 suspect cluster Cepheids, listed in Table 8 and shown in Figure 12 (Appendix B). Three of them (01343182+3043050, 01343169+3043002, and 01340910+3036296) are listed in the Johnson et al. (2022) catalog, but at a distance greater than $1.2 r_{ap}$ from the Cepheid (on average at $\sim 2 r_{ap}$); therefore, they were not found by the crossmatch procedure. Two of them are also listed in the Sarajedini & Mancone (2007) catalog at about $1''$ and $4''.5$ from the Cepheid (this catalog does not provide the cluster radii).

5.5. Flux Contribution from the Clusters

We followed the approach used in Anderson & Riess (2018; see their Section 3.2.1) to separate three contributions: the flux from the Cepheid, the flux of the cluster, and the background contribution. The average cumulative light contribution from clusters Δm (or curve of growth) is obtained using a series of apertures of increasing radius, starting from the Cepheid in the center ($r = 1$ pixel) to a radius of about $2''$. We note that Δm can be negative (if a light contribution from the cluster is detected) or positive (if the cluster flux is low or if its location is statistically sparser than the nearby environment of the Cepheid). At the distance to M33 found in Section 4.5, a separation of $1''$ corresponds to 4.1 pc along the major axis and 3.7 pc along the minor axis as projected on the plane of the disk. Anderson & Riess (2018) find that the cluster light contribution in M31 flattens off at a separation of about 3.8 pc, which corresponds to approximately twice the average cluster radius.

Table 8
Cluster Cepheids Found by Inspecting Visually the Image Cutouts from PHATTER Mosaics Centered on Each Cepheid

Cepheid	Cluster	r_{ap} ($''$)	θ_{sep} ($''$)
01333896+3034140	–	–	–
01343182+3043050	J22-40	1.60	3.73
01333015+3038039	–	–	–
01333438+3035307	–	–	–
01333433+3034270	–	–	–
01343169+3043002	J22-40	1.60	2.96
01340910+3036296	J22-27, S07-325	2.23	4.71
01341217+3036362	–	–	–
01340474+3049181	S07-292	–	1.12
01333348+3033210	–	–	–
01334821+3038001	–	–	–
01342988+3047541	–	–	–
01340084+3049551	–	–	–

Note. The second column indicates if the Cepheid is found nearby a cluster listed in J22 or in S07, and "–" indicates that no known cluster was found around this Cepheid in the literature.

Figure 9 shows the average light contribution from the 10 confirmed M33 clusters (Section 5.2, Table 7). Similarly to Anderson & Riess (2018), the contribution in the optical is significant, with Δm around -0.5 mag in F475W at a separation of 4 pc, and becomes lower toward the NIR with $\Delta m = -0.20$ mag and -0.17 mag in F814W and m_H^W, respectively. These values are about a factor of 2 smaller than those found by Anderson & Riess (2018) in M31 at the same separation.

The contribution of the 13 additional cluster Cepheids obtained by visual inspection of the stamp images (Section 5.4, Table 8) is represented in Figure 10. In all filters, it is lower than the contribution from the 10 confirmed clusters (Figure 9) with only $\Delta m = -0.02$ mag at 4 pc in m_H^W. This suggests that the 13 additional possible cluster Cepheids do not contribute to the contamination of the Cepheid flux.

Following Anderson & Riess (2018), we estimate the average photometric bias produced by the 10 confirmed cluster Cepheids from Table 7 by multiplying their occurrence rate (1.6%) by their flux contribution in m_H^W, which gives a bias of 0.003 mag. This shows that cluster Cepheids do not impact the distance measurement of M33. If we conservatively assume that all 13 additional Cepheids from Table 8 are associated with clusters, we obtain a maximum occurrence rate of 3.7%, which is still lower than the fraction of cluster Cepheids in the Milky Way, LMC, and SMC, and a correspondingly lower bias per cluster Cepheid (since the additional 13 do not produce a significant difference).

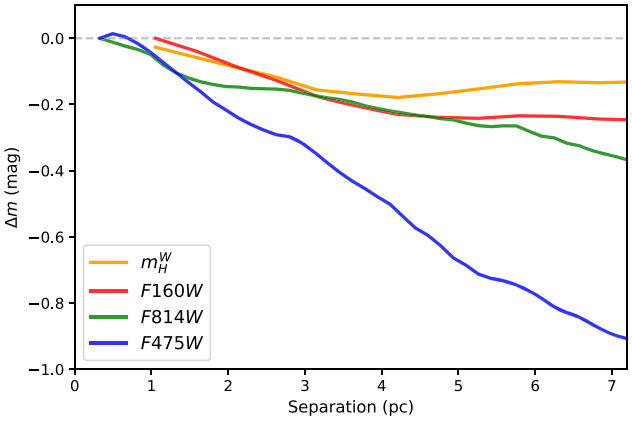

Figure 9. Average cluster contribution (curve of growth) for the 10 confirmed M33 cluster Cepheids (Table 7) in the m_H^W, F160W, F475W, and F814W filters.

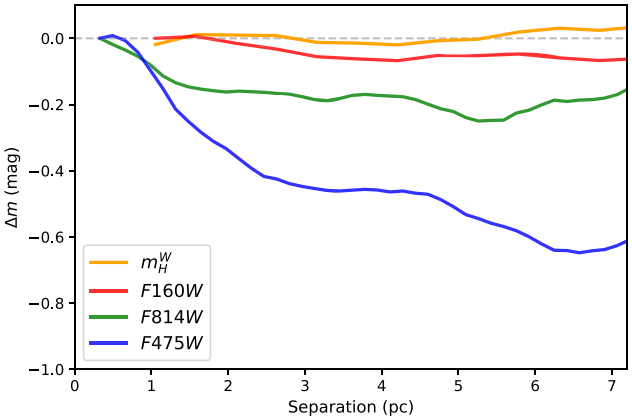

Figure 10. Average cluster contribution (curve of growth) for the 13 additional cluster Cepheids found by visual inspection (Table 8) in the m_H^W, F160W, F475W, and F814W filters.

6. Summary

We take advantage of the recently published high-quality PHATTER photometric survey of the M33 galaxy and we construct the Cepheid PL relation in the SH0ES NIR Wesenheit system (m_H^W). We use well-sampled ground-based light curves for the same Cepheid sample to recover the phases and amplitudes and we correct the random-epoch PHATTER measurements to mean magnitude. We also present new optical template light curves based on the same population of M33 Cepheids. These can be directly applied to fit sparsely sampled light curves.

We improve the uncertainty in the Cepheid distance to M33 to the 1.3% level and we present the tightest PL relation to date in this galaxy, with a scatter of only 0.11 mag. In particular, the use of HST photometry allows us to significantly reduce the effect of crowding over past studies based on ground-based observations. This new Cepheid distance provides the groundwork for including M33 as an anchor galaxy in the empirical distance scale (Riess et al. 2022), with a similar role as the Milky Way, the LMC, and NGC 4258. In order to consider M33 as an independent anchor of the distance scale, a precise geometric calibration of its distance is required, using, for example, a large sample of late-type DEBs. Future facilities, such as the Extremely Large Telescope and the Roman Space Telescope, could enable significant improvements in that matter.

We discuss differences between past measurements of the distance to M33, especially based on the TRGB method, and we identify factors that explain these discrepancies, such as the possible effect of blending and the choice of color cut when defining the red giant branch in the color–magnitude diagram. Finally, we investigate the bias from cluster Cepheids and estimate that at most 3.7% of M33 Cepheids are in these systems, resulting in a negligible contamination of 0.003 mag to our distance measurement. Our result, compared with other distance measurements from the literature, highlights the unprecedented reliability and precision of Cepheids as standard candles.

Acknowledgments

We thank Abigail Lee for discussions about the TRGB and Cepheid distances to M33. L.B. is deeply grateful to Arshia Jacob for her constant support and kindness during the preparation of this paper. This research has made use of Astropy, a community-developed core Python package for Astronomy (Astropy Collaboration et al. 2018), as well as of the SVO Filter Profile Service.[10] Some of the data presented in this paper were obtained from the Mikulski Archive for Space Telescopes (MAST) at the STScI.

Appendix A
Output Parameters for HST M33 Cepheids

Table 9 lists the final parameters obtained for our sample of M33 Cepheids.

[10] http://svo2.cab.inta- csic.es/theory/fps/

Table 9
Full Sample of HST M33 Cepheids Used in This Analysis and Their Mean Magnitudes Obtained from Template Fitting

ID	R.A.	Decl.	log P	F160W	F475W	F814W	m_H^W	d_{GC}	Δ_{corr}	Sample
01332610+3033200	23.35862	30.55548	1.301	$18.261_{(91)}$	$20.678_{(79)}$	$19.171_{(24)}$	$17.853_{(93)}$	2.45	−0.002	G
01332735+3035515	23.36379	30.59756	1.050	$19.154_{(71)}$	$21.093_{(84)}$	$19.791_{(46)}$	$18.798_{(75)}$	2.39	−0.003	G
01332768+3034238(*)	23.36521	30.57321	1.171	$18.402_{(53)}$	$20.330_{(35)}$	$19.103_{(35)}$	$18.065_{(54)}$	2.29	−0.002	G
01332803+3032133	23.36666	30.53703	1.197	$18.575_{(79)}$	$21.810_{(113)}$	$19.868_{(37)}$	$18.057_{(85)}$	2.36	−0.002	G
01332878+3034403	23.36978	30.57779	0.949	$19.179_{(34)}$	$20.922_{(38)}$	$19.891_{(37)}$	$18.892_{(37)}$	2.18	−0.002	G
01332922+3031360	23.37160	30.52666	0.815	$19.920_{(45)}$	$21.726_{(62)}$	$20.463_{(51)}$	$19.574_{(49)}$	2.35	−0.001	G
01332923+3037449	23.37169	30.62909	1.663	$16.942_{(165)}$	$20.028_{(50)}$	$18.235_{(14)}$	$16.462_{(166)}$	2.38	−0.003	G
01332946+3035574	23.37261	30.59925	1.487	$17.655_{(116)}$	$20.634_{(125)}$	$18.886_{(156)}$	$17.186_{(127)}$	2.16	−0.003	G
01332984+3034529	23.37420	30.58129	0.908	$19.398_{(44)}$	$21.553_{(87)}$	$20.243_{(8)}$	$19.040_{(49)}$	2.07	−0.002	G
01333012+3036381	23.37536	30.61055	1.255	$18.325_{(144)}$	$20.271_{(25)}$	$18.926_{(11)}$	$17.958_{(144)}$	2.13	−0.003	G
01333039+3035555	23.37647	30.59870	1.344	$17.940_{(132)}$	$20.124_{(15)}$	$18.725_{(20)}$	$17.560_{(132)}$	2.05	−0.002	G
01333073+3034495	23.37792	30.58036	0.749	$19.809_{(102)}$	$21.667_{(13)}$	$20.567_{(43)}$	$19.505_{(103)}$	1.98	−0.002	G
01333080+3031113	23.37816	30.51978	1.244	$18.372_{(134)}$	$20.982_{(174)}$	$19.409_{(111)}$	$17.947_{(144)}$	2.34	−0.001	G
01333165+3039314	23.38172	30.65870	1.119	$18.743_{(172)}$	$20.180_{(26)}$	$19.316_{(173)}$	$18.498_{(178)}$	2.38	−0.004	S
01333216+3039457	23.38386	30.66268	1.175	$18.712_{(81)}$	$21.129_{(223)}$	$19.564_{(160)}$	$18.289_{(107)}$	2.37	−0.004	G
01333241+3031437	23.38487	30.52878	0.901	$19.506_{(171)}$	$21.925_{(108)}$	$20.460_{(15)}$	$19.109_{(173)}$	2.17	−0.001	S
01333242+3034094	23.38492	30.56924	0.848	$19.545_{(76)}$	$20.997_{(127)}$	$20.087_{(86)}$	$19.289_{(85)}$	1.85	−0.001	G
01333291+3035490	23.38696	30.59689	1.481	$17.557_{(138)}$	$20.698_{(181)}$	$18.914_{(156)}$	$17.079_{(151)}$	1.77	−0.002	G
01333308+3042308	23.38768	30.70852	0.779	$19.828_{(198)}$	$21.925_{(115)}$	$20.678_{(235)}$	$19.486_{(209)}$	2.91	−0.004	S
01333327+3037476	23.38846	30.62985	1.355	$18.266_{(174)}$	$21.417_{(394)}$	$19.512_{(194)}$	$17.757_{(207)}$	1.88	−0.003	S
01333348+3033210(*)	23.38935	30.55578	0.955	$19.300_{(200)}$	$21.277_{(13)}$	$20.067_{(57)}$	$18.968_{(201)}$	1.86	−0.001	S
01333424+3035009	23.39251	30.58353	1.196	$18.629_{(82)}$	$21.051_{(312)}$	$19.664_{(171)}$	$18.252_{(122)}$	1.65	−0.001	G
01333438+3035307 (*)	23.39314	30.59179	1.200	$18.459_{(143)}$	$20.760_{(263)}$	$19.367_{(109)}$	$18.080_{(160)}$	1.61	−0.002	S
01333548+3044180	23.39767	30.73833	0.978	$19.173_{(35)}$	$21.503_{(167)}$	$20.039_{(106)}$	$18.776_{(61)}$	3.12	−0.005	G
01333552+3033307	23.39782	30.55848	1.062	$18.869_{(85)}$	$21.022_{(11)}$	$19.710_{(10)}$	$18.511_{(85)}$	1.72	−0.001	G
01333557+3036496	23.39802	30.61376	1.029	$19.166_{(52)}$	$21.463_{(211)}$	$20.072_{(104)}$	$18.788_{(79)}$	1.51	−0.002	G
01333628+3037313	23.40097	30.62529	1.071	$19.110_{(35)}$	$21.900_{(37)}$	$20.144_{(29)}$	$18.639_{(37)}$	1.48	−0.002	G
01333649+3030536	23.40196	30.51484	0.880	$19.243_{(81)}$	$20.923_{(227)}$	$20.045_{(140)}$	$18.995_{(106)}$	2.28	0.001	G
01333680+3034348	23.40312	30.57629	0.957	$19.254_{(41)}$	$20.811_{(166)}$	$19.752_{(52)}$	$18.960_{(60)}$	1.49	−0.001	G
01333747+3031388	23.40594	30.52741	1.761	$16.988_{(84)}$	$20.102_{(136)}$	$18.180_{(73)}$	$16.475_{(93)}$	2.08	0.000	G
01333754+3033054	23.40619	30.55145	0.953	$19.297_{(27)}$	$21.627_{(70)}$	$20.234_{(23)}$	$18.918_{(33)}$	1.73	−0.000	S
01333791+3033550	23.40781	30.56522	0.952	$19.418_{(200)}$	$21.500_{(75)}$	$20.205_{(40)}$	$19.064_{(201)}$	1.55	−0.000	S
01333880+3037515	23.41152	30.63090	1.139	$18.981_{(69)}$	$21.503_{(25)}$	$19.875_{(30)}$	$18.542_{(70)}$	1.21	−0.002	G
01334058+3045421	23.41889	30.76168	0.868	$19.584_{(69)}$	$21.989_{(211)}$	$20.444_{(138)}$	$19.166_{(94)}$	2.97	−0.004	G
01334167+3043115	23.42343	30.71983	0.906	$19.402_{(209)}$	$21.789_{(27)}$	$20.397_{(40)}$	$19.023_{(209)}$	2.07	−0.003	S
01334331+3043559 (*)	23.43035	30.73221	1.305	$18.196_{(123)}$	$20.940_{(70)}$	$19.246_{(92)}$	$17.741_{(126)}$	2.12	−0.003	G
01334390+3032452	23.43275	30.54584	1.873	$16.197_{(91)}$	$19.803_{(55)}$	$17.745_{(31)}$	$15.649_{(92)}$	1.89	0.001	G
01334456+3043132	23.43546	30.72032	1.351	$18.135_{(76)}$	$20.891_{(68)}$	$19.202_{(31)}$	$17.681_{(78)}$	1.76	−0.002	G
01334582+3044207	23.44076	30.73905	1.118	$18.983_{(94)}$	$21.239_{(90)}$	$19.893_{(13)}$	$18.616_{(97)}$	1.99	−0.003	G
01334596+3030303	23.44137	30.50840	0.538	$20.445_{(87)}$	$22.468_{(246)}$	$21.529_{(81)}$	$20.181_{(109)}$	2.72	0.003	G
01334654+3046449	23.44378	30.77914	1.274	$18.341_{(104)}$	$20.247_{(53)}$	$18.945_{(26)}$	$17.985_{(105)}$	2.70	−0.003	G
01334681+3043335	23.44491	30.72595	0.778	$19.771_{(64)}$	$21.715_{(136)}$	$20.578_{(112)}$	$19.457_{(78)}$	1.63	−0.002	G
01334691+3044112	23.44533	30.73646	0.750	$19.852_{(132)}$	$22.002_{(8)}$	$20.699_{(19)}$	$19.496_{(132)}$	1.83	−0.002	S
01334720+3035365	23.44651	30.59341	1.423	$17.767_{(110)}$	$20.319_{(154)}$	$18.804_{(8)}$	$17.357_{(117)}$	1.13	0.001	G
01334821+3038001 (*)	23.45071	30.63334	1.178	$18.557_{(115)}$	$20.428_{(20)}$	$19.166_{(25)}$	$18.211_{(115)}$	0.43	0.000	G
01334879+3049143	23.45313	30.82062	0.749	$19.980_{(47)}$	$21.885_{(71)}$	$20.668_{(43)}$	$19.646_{(52)}$	3.33	−0.004	G
01334886+3034159	23.45342	30.57106	0.901	$19.351_{(41)}$	$21.181_{(191)}$	$20.118_{(71)}$	$19.056_{(66)}$	1.67	0.002	G
01334929+3032182	23.45520	30.53832	0.991	$19.302_{(175)}$	$21.790_{(62)}$	$20.264_{(33)}$	$18.889_{(176)}$	2.35	0.003	S
01334955+3047437	23.45627	30.79547	0.779	$19.902_{(46)}$	$21.931_{(78)}$	$20.721_{(54)}$	$19.570_{(52)}$	2.76	−0.003	G
01334960+3044008	23.45654	30.73355	0.798	$19.742_{(38)}$	$21.926_{(113)}$	$20.697_{(15)}$	$19.405_{(48)}$	1.52	−0.002	G
01334983+3037587	23.45749	30.63294	1.111	$18.690_{(110)}$	$20.738_{(20)}$	$19.470_{(20)}$	$18.343_{(110)}$	0.51	0.001	G
01335051+3047537	23.46029	30.79822	1.423	$17.912_{(104)}$	$20.897_{(116)}$	$19.077_{(79)}$	$17.425_{(110)}$	2.74	−0.003	G
01335067+3034459	23.46094	30.57936	0.780	$19.842_{(207)}$	$22.022_{(340)}$	$20.689_{(218)}$	$19.478_{(231)}$	1.64	0.002	S
01335067+3047146	23.46098	30.78735	0.987	$19.088_{(46)}$	$21.349_{(240)}$	$20.036_{(90)}$	$18.729_{(80)}$	2.51	−0.003	G
01335075+3035444	23.46134	30.59562	1.368	$18.191_{(120)}$	$20.776_{(20)}$	$19.121_{(20)}$	$17.746_{(120)}$	1.32	0.002	G
01335090+3033361	23.46191	30.56000	1.575	$17.638_{(60)}$	$21.241_{(201)}$	$19.103_{(94)}$	$17.070_{(82)}$	2.05	0.002	G
01335094+3031174	23.46212	30.52141	0.678	$19.998_{(40)}$	$21.830_{(55)}$	$20.726_{(26)}$	$19.693_{(43)}$	2.82	0.003	G
01335104+3043598	23.46256	30.73322	1.091	$18.935_{(74)}$	$21.353_{(137)}$	$19.833_{(102)}$	$18.524_{(86)}$	1.40	−0.002	G
01335172+3050370	23.46538	30.84358	0.956	$19.405_{(200)}$	$21.505_{(483)}$	$20.209_{(226)}$	$19.051_{(242)}$	3.55	−0.004	S
01335182+3033109	23.46575	30.55295	0.813	$19.753_{(18)}$	$22.289_{(9)}$	$20.764_{(43)}$	$19.341_{(21)}$	2.26	0.003	G
01335198+3048485	23.46642	30.81345	1.125	$18.920_{(172)}$	$20.610_{(215)}$	$19.459_{(142)}$	$18.603_{(184)}$	2.93	−0.003	S
01335232+3046026	23.46785	30.76738	0.775	$19.957_{(294)}$	$22.292_{(24)}$	$20.793_{(240)}$	$19.551_{(300)}$	1.99	−0.002	S
01335247+3038442	23.46850	30.64558	1.554	$17.443_{(139)}$	$19.865_{(80)}$	$18.448_{(20)}$	$17.058_{(141)}$	0.51	0.001	G
01335311+3048343 (*)	23.47112	30.80947	0.982	$19.156_{(174)}$	$20.813_{(401)}$	$19.761_{(138)}$	$18.864_{(205)}$	2.77	−0.003	S

Table 9
(Continued)

ID	R.A.	Decl.	log P	F160W	F475W	F814W	m_H^W	d_{GC}	Δ_{corr}	Sample
01335345+3033085	23.47257	30.55231	1.061	$19.106_{(60)}$	$21.593_{(71)}$	$20.079_{(78)}$	$18.696_{(66)}$	2.42	0.003	G
01335428+3041107	23.47605	30.68626	1.448	$17.642_{(165)}$	$20.302_{(123)}$	$18.699_{(64)}$	$17.210_{(169)}$	0.45	0.000	G
01335478+3041061	23.47812	30.68499	1.531	$17.420_{(105)}$	$20.191_{(13)}$	$18.479_{(6)}$	$16.960_{(105)}$	0.47	0.000	G
01335479+3045181	23.47817	30.75501	0.762	$19.692_{(198)}$	$21.582_{(59)}$	$20.474_{(33)}$	$19.385_{(199)}$	1.60	−0.001	S
01335482+3045317	23.47827	30.75880	1.553	$17.543_{(99)}$	$19.167_{(279)}$	$17.781_{(18)}$	$17.166_{(122)}$	1.67	−0.001	G
01335502+3035372	23.47909	30.59359	1.006	$19.054_{(68)}$	$21.186_{(8)}$	$19.907_{(22)}$	$18.704_{(68)}$	1.77	0.002	G
01335514+3048309	23.47962	30.80854	0.949	$19.528_{(200)}$	$21.798_{(516)}$	$20.328_{(282)}$	$19.130_{(250)}$	2.62	−0.002	S
01335523+3043429	23.47998	30.72855	1.421	$18.011_{(232)}$	$20.786_{(454)}$	$19.056_{(117)}$	$17.547_{(261)}$	1.09	−0.001	S
01335612+3039029	23.48372	30.65077	1.018	$19.106_{(56)}$	$21.335_{(18)}$	$19.998_{(18)}$	$18.741_{(56)}$	0.87	0.001	G
01335615+3043424	23.48382	30.72840	1.078	$18.951_{(58)}$	$21.309_{(37)}$	$19.795_{(77)}$	$18.541_{(62)}$	1.07	−0.000	G
01335645+3046435	23.48506	30.77878	0.863	$19.646_{(75)}$	$21.755_{(20)}$	$20.370_{(24)}$	$19.269_{(75)}$	1.98	−0.001	G
01335646+3044420	23.48506	30.74492	0.739	$19.847_{(103)}$	$21.739_{(117)}$	$20.702_{(105)}$	$19.559_{(110)}$	1.35	−0.001	G
01335737+3041133	23.48894	30.68700	1.065	$18.885_{(172)}$	$21.487_{(54)}$	$19.907_{(46)}$	$18.459_{(173)}$	0.71	0.001	S
01335760+3048341	23.48978	30.80942	0.685	$20.248_{(54)}$	$22.664_{(203)}$	$21.193_{(107)}$	$19.849_{(79)}$	2.51	−0.002	G
01335761+3038053	23.48990	30.63479	1.092	$18.852_{(172)}$	$21.290_{(128)}$	$19.790_{(230)}$	$18.446_{(185)}$	1.31	0.002	S
01335809+3045568 (*)	23.49190	30.76576	1.499	$17.818_{(228)}$	$20.706_{(204)}$	$18.935_{(118)}$	$17.343_{(236)}$	1.68	−0.001	S
01335852+3043596	23.49375	30.73320	1.047	$18.905_{(52)}$	$21.599_{(182)}$	$20.026_{(23)}$	$18.480_{(70)}$	1.15	−0.000	G
01335870+3033166	23.49445	30.55457	0.886	$19.371_{(43)}$	$21.328_{(58)}$	$20.094_{(59)}$	$19.032_{(48)}$	2.90	0.004	G
01335886+3037198	23.49510	30.62213	1.390	$18.027_{(179)}$	$20.603_{(114)}$	$19.116_{(70)}$	$17.624_{(182)}$	1.67	0.002	G
01335947+3032266	23.49765	30.54068	1.699	$17.186_{(67)}$	$20.559_{(35)}$	$18.604_{(24)}$	$16.664_{(68)}$	3.25	0.004	G
01335989+3037600	23.49941	30.63331	0.778	$19.916_{(70)}$	$21.263_{(121)}$	$20.381_{(76)}$	$19.667_{(79)}$	1.61	0.002	G
01340058+3036306	23.50228	30.60846	0.802	$19.643_{(195)}$	$21.814_{(119)}$	$20.535_{(63)}$	$19.293_{(198)}$	2.12	0.003	S
01340102+3043097	23.50412	30.71935	1.484	$17.804_{(108)}$	$20.225_{(351)}$	$18.811_{(135)}$	$17.420_{(144)}$	1.12	0.001	G
01340120+3048131	23.50483	30.80360	0.665	$20.350_{(221)}$	$22.574_{(358)}$	$21.258_{(141)}$	$19.991_{(242)}$	2.28	−0.001	S
01340123+3031135	23.50497	30.52038	1.396	$17.746_{(83)}$	$19.537_{(253)}$	$18.430_{(143)}$	$17.440_{(111)}$	3.82	0.005	G
01340137+3040264	23.50558	30.67394	1.174	$18.586_{(174)}$	$21.979_{(165)}$	$20.129_{(241)}$	$18.091_{(189)}$	1.26	0.002	S
01340166+3031030	23.50674	30.51745	1.198	$18.359_{(116)}$	$21.288_{(331)}$	$19.544_{(140)}$	$17.891_{(148)}$	3.92	0.005	G
01340167+3049102	23.50679	30.81947	0.631	$20.286_{(35)}$	$21.956_{(64)}$	$20.970_{(50)}$	$20.010_{(41)}$	2.55	−0.001	G
01340178+3039229	23.50727	30.65632	1.336	$18.084_{(112)}$	$20.439_{(133)}$	$18.936_{(144)}$	$17.677_{(123)}$	1.52	0.002	G
01340187+3041483	23.50768	30.69674	0.802	$19.859_{(55)}$	$21.689_{(209)}$	$20.572_{(90)}$	$19.550_{(80)}$	1.18	0.001	G
01340219+3037418	23.50897	30.62823	0.864	$19.655_{(38)}$	$21.206_{(156)}$	$20.198_{(84)}$	$19.374_{(59)}$	1.98	0.003	G
01340223+3042423	23.50917	30.71173	0.894	$19.331_{(89)}$	$21.406_{(12)}$	$20.082_{(8)}$	$18.970_{(89)}$	1.20	0.001	G
01340259+3036282	23.51068	30.60780	1.135	$18.887_{(174)}$	$21.318_{(85)}$	$19.763_{(37)}$	$18.467_{(176)}$	2.37	0.004	S
01340296+3047273	23.51222	30.79088	0.850	$19.550_{(79)}$	$21.515_{(64)}$	$20.337_{(35)}$	$19.226_{(81)}$	2.05	−0.000	G
01340367+3045279	23.51516	30.75769	0.792	$19.820_{(90)}$	$21.371_{(102)}$	$20.329_{(38)}$	$19.530_{(94)}$	1.61	0.000	G
01340399+3036158	23.51651	30.60435	1.211	$18.389_{(104)}$	$20.650_{(206)}$	$19.251_{(26)}$	$18.009_{(117)}$	2.60	0.004	G
01340426+3041150	23.51763	30.68746	0.882	$19.441_{(48)}$	$21.748_{(177)}$	$20.336_{(124)}$	$19.057_{(73)}$	1.51	0.002	G
01340501+3035576	23.52076	30.59927	0.770	$19.777_{(49)}$	$21.702_{(53)}$	$20.524_{(48)}$	$19.453_{(52)}$	2.81	0.004	G
01340516+3038511	23.52135	30.64750	1.842	$16.855_{(118)}$	$19.970_{(634)}$	$18.018_{(358)}$	$16.334_{(219)}$	2.07	0.003	S
01340593+3038192	23.52458	30.63865	1.031	$19.197_{(172)}$	$21.720_{(317)}$	$20.192_{(179)}$	$18.784_{(195)}$	2.29	0.003	S
01340593+3039285	23.52457	30.65787	1.164	$18.491_{(174)}$	$20.841_{(468)}$	$19.413_{(299)}$	$18.103_{(224)}$	2.03	0.003	S
01340660+3038167	23.52732	30.63792	0.934	$19.195_{(200)}$	$21.178_{(190)}$	$19.912_{(70)}$	$18.848_{(207)}$	2.39	0.004	S
01340737+3030483	23.53053	30.51340	0.771	$19.957_{(62)}$	$22.091_{(109)}$	$20.796_{(38)}$	$19.603_{(69)}$	4.62	0.007	G
01340794+3038312	23.53295	30.64201	0.771	$19.805_{(198)}$	$21.712_{(196)}$	$20.526_{(218)}$	$19.479_{(212)}$	2.50	0.004	S
01340817+3039318	23.53385	30.65881	1.125	$18.857_{(172)}$	$21.385_{(80)}$	$19.963_{(70)}$	$18.471_{(174)}$	2.30	0.003	S
01340873+3045431	23.53626	30.76194	1.131	$18.535_{(113)}$	$20.827_{(135)}$	$19.432_{(111)}$	$18.156_{(121)}$	1.94	0.001	G
01340883+3039462	23.53665	30.66281	1.005	$19.132_{(42)}$	$21.307_{(7)}$	$19.944_{(8)}$	$18.761_{(42)}$	2.34	0.004	G
01340910+3036296 (*)	23.53775	30.60817	1.165	$18.426_{(174)}$	$20.352_{(361)}$	$19.193_{(202)}$	$18.107_{(203)}$	3.16	0.005	S
01340936+3029565	23.53888	30.49902	0.962	$19.283_{(26)}$	$21.328_{(53)}$	$20.057_{(33)}$	$18.935_{(30)}$	5.11	0.007	G
01340959+3036215 (*)	23.53982	30.60592	1.021	$18.932_{(175)}$	$21.144_{(206)}$	$19.881_{(108)}$	$18.586_{(185)}$	3.26	0.005	S
01341017+3044502	23.54226	30.74722	1.018	$19.253_{(53)}$	$21.528_{(143)}$	$20.131_{(70)}$	$18.873_{(67)}$	2.00	0.002	G
01341027+3034077	23.54264	30.56876	1.287	$18.334_{(12)}$	$21.147_{(79)}$	$19.530_{(5)}$	$17.898_{(23)}$	3.96	0.006	G
01341121+3047547	23.54658	30.79851	1.094	$18.753_{(173)}$	$20.646_{(18)}$	$19.484_{(13)}$	$18.433_{(173)}$	2.37	0.001	S
01341125+3041558	23.54670	30.69881	1.425	$17.682_{(98)}$	$20.116_{(51)}$	$18.659_{(21)}$	$17.287_{(99)}$	2.29	0.003	G
01341199+3035191	23.54984	30.58858	1.126	$18.879_{(173)}$	$21.201_{(114)}$	$19.759_{(275)}$	$18.488_{(189)}$	3.84	0.006	S
01341217+3036362 (*)	23.55054	30.61004	1.215	$18.569_{(112)}$	$21.245_{(114)}$	$19.628_{(61)}$	$18.133_{(117)}$	3.51	0.005	G
01341217+3046411	23.55057	30.77806	1.555	$17.423_{(92)}$	$19.816_{(88)}$	$18.420_{(52)}$	$17.043_{(96)}$	2.28	0.002	G
01341226+3045507	23.55094	30.76406	1.001	$19.118_{(175)}$	$21.574_{(443)}$	$20.049_{(282)}$	$18.706_{(220)}$	2.23	0.002	S
01341241+3047206	23.55159	30.78903	0.631	$20.278_{(193)}$	$22.276_{(83)}$	$21.049_{(77)}$	$19.941_{(195)}$	2.37	0.001	S
01341259+3041262	23.55229	30.69057	0.920	$19.430_{(26)}$	$21.757_{(20)}$	$20.309_{(35)}$	$19.037_{(28)}$	2.52	0.004	G
01341330+3043069	23.55525	30.71855	0.932	$19.396_{(200)}$	$21.851_{(64)}$	$20.358_{(19)}$	$18.992_{(201)}$	2.40	0.003	S
01341343+3043340	23.55581	30.72608	0.961	$19.237_{(178)}$	$21.420_{(85)}$	$20.042_{(12)}$	$18.862_{(179)}$	2.38	0.003	S
01341356+3030274	23.55638	30.50760	0.864	$19.575_{(35)}$	$21.689_{(40)}$	$20.395_{(15)}$	$19.221_{(37)}$	5.43	0.008	G
01341383+3044184	23.55748	30.73844	1.026	$19.302_{(172)}$	$21.796_{(4)}$	$20.255_{(15)}$	$18.886_{(172)}$	2.39	0.003	S

Table 9
(Continued)

ID	R.A.	Decl.	$\log P$	F160W	F475W	F814W	m_H^W	d_{GC}	Δ_{corr}	Sample
01341387+3043240	23.55763	30.72327	0.901	$19.461_{(23)}$	$21.780_{(59)}$	$20.371_{(40)}$	$19.078_{(29)}$	2.45	0.003	G
01341389+3032122	23.55768	30.53665	0.959	$19.283_{(200)}$	$21.671_{(395)}$	$20.240_{(297)}$	$18.894_{(236)}$	4.95	0.007	S
01341396+3048375	23.55800	30.81037	0.753	$19.938_{(66)}$	$21.839_{(73)}$	$20.739_{(80)}$	$19.634_{(72)}$	2.63	0.001	G
01341425+3037138	23.55915	30.62045	0.977	$19.220_{(30)}$	$21.670_{(142)}$	$20.195_{(86)}$	$18.820_{(52)}$	3.61	0.005	G
01341471+3046097	23.56121	30.76937	1.071	$19.099_{(172)}$	$22.208_{(413)}$	$20.344_{(227)}$	$18.600_{(210)}$	2.47	0.002	S
01341554+3044116	23.56461	30.73654	0.909	$19.562_{(38)}$	$21.784_{(8)}$	$20.333_{(5)}$	$19.168_{(38)}$	2.58	0.003	G
01341590+3046436	23.56614	30.77876	0.932	$19.414_{(34)}$	$21.830_{(103)}$	$20.383_{(12)}$	$19.021_{(43)}$	2.60	0.002	G
01341889+3044412	23.57860	30.74478	1.305	$18.464_{(128)}$	$20.761_{(82)}$	$19.349_{(12)}$	$18.080_{(130)}$	2.93	0.004	G
01341986+3043020	23.58260	30.71719	0.916	$19.538_{(200)}$	$21.899_{(69)}$	$20.437_{(300)}$	$19.142_{(215)}$	3.21	0.004	S
01342038+3041010	23.58481	30.68358	1.203	$18.613_{(137)}$	$20.968_{(43)}$	$19.449_{(50)}$	$18.202_{(138)}$	3.59	0.005	G
01342055+3042440	23.58546	30.71216	0.756	$19.795_{(85)}$	$21.595_{(163)}$	$20.508_{(51)}$	$19.494_{(95)}$	3.33	0.005	G
01342102+3044152	23.58745	30.73754	0.999	$19.168_{(175)}$	$20.997_{(472)}$	$19.778_{(172)}$	$18.833_{(217)}$	3.22	0.004	S
01342122+3045369	23.58828	30.76025	1.251	$18.207_{(86)}$	$20.391_{(159)}$	$19.101_{(81)}$	$17.854_{(97)}$	3.14	0.004	G
01342142+3046180	23.58915	30.77163	0.677	$20.039_{(58)}$	$22.129_{(16)}$	$20.885_{(7)}$	$19.698_{(58)}$	3.14	0.004	G
01342241+3044080	23.59329	30.73553	0.884	$19.570_{(145)}$	$21.678_{(29)}$	$20.345_{(16)}$	$19.206_{(145)}$	3.40	0.005	S
01342254+3049055	23.59378	30.81818	1.297	$18.214_{(185)}$	$20.823_{(619)}$	$19.201_{(38)}$	$17.777_{(243)}$	3.30	0.003	S
01342419+3047389	23.60070	30.79412	0.886	$19.420_{(111)}$	$21.220_{(102)}$	$20.113_{(52)}$	$19.114_{(115)}$	3.41	0.004	G
01342472+3044311	23.60284	30.74196	0.771	$19.964_{(198)}$	$21.907_{(19)}$	$20.703_{(2)}$	$19.633_{(198)}$	3.63	0.005	S
01342913+3043388	23.62126	30.72743	1.169	$18.850_{(174)}$	$19.794_{(562)}$	$18.908_{(197)}$	$18.600_{(231)}$	4.28	0.006	S
01343020+3044567	23.62573	30.74908	0.603	$20.372_{(29)}$	$22.500_{(106)}$	$21.224_{(34)}$	$20.023_{(41)}$	4.25	0.006	G
01342988+3047541 (*)	23.62439	30.79834	1.090	$19.015_{(172)}$	$21.594_{(318)}$	$19.990_{(151)}$	$18.583_{(194)}$	4.00	0.005	S
01335230+3045008	23.46777	30.75023	0.964	$19.338_{(200)}$	$21.840_{(293)}$	$20.273_{(265)}$	$18.915_{(224)}$	1.65	−0.002	S
01334228+3037474	23.42596	30.62976	1.193	$18.734_{(185)}$	$20.824_{(25)}$	$19.411_{(20)}$	$18.350_{(185)}$	0.82	−0.001	S
01341344+3033177	23.55582	30.55488	1.060	$18.898_{(173)}$	$21.533_{(28)}$	$20.041_{(298)}$	$18.494_{(189)}$	4.58	0.007	S
01333576+3033007	23.39879	30.55014	0.780	$19.765_{(199)}$	$21.964_{(352)}$	$20.697_{(167)}$	$19.418_{(222)}$	1.80	−0.000	S
01333825+3042510	23.40920	30.71414	0.906	$19.378_{(200)}$	$21.799_{(69)}$	$20.407_{(5)}$	$18.999_{(201)}$	2.38	−0.004	S

Notes. The errors are given in millimagnitudes in the brackets. The values here do not include the subtraction of 0.015 mag to correct CRNL for 2 dex between LMC and M33 Cepheids and they do not include the addition of 0.069 mag to m_H^W errors for the intrinsic scatter. The deprojected galactocentric distance d_{GC} (in kpc) and the geometric correction Δ_{corr} (in mag) are listed in the 9th and 10th columns. The sample names in the last column are: (G) = gold and (S) = silver. Cepheids marked with (*) are listed as cluster Cepheids in Section 5.

(This table is available in machine-readable form.)

Appendix B
Postage Stamps of Cluster Cepheids

Figures 11 and 12, respectively, show the HST postage stamps of the confirmed and suspected cluster Cepheids in M33.

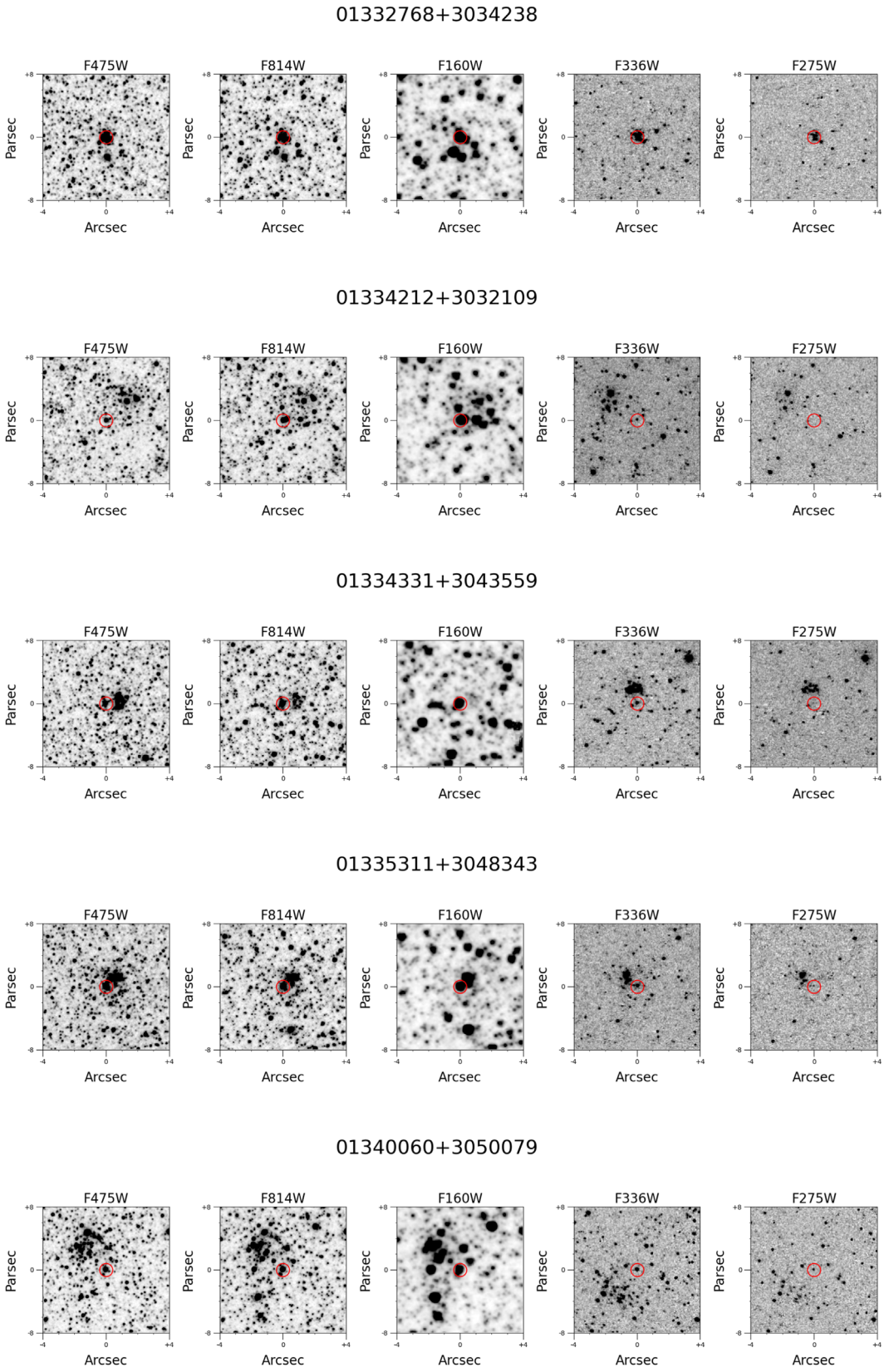

Figure 11. Postage stamps in HST filters for the 10 Cluster Cepheids detected by the crossmatch procedure (Section 5).

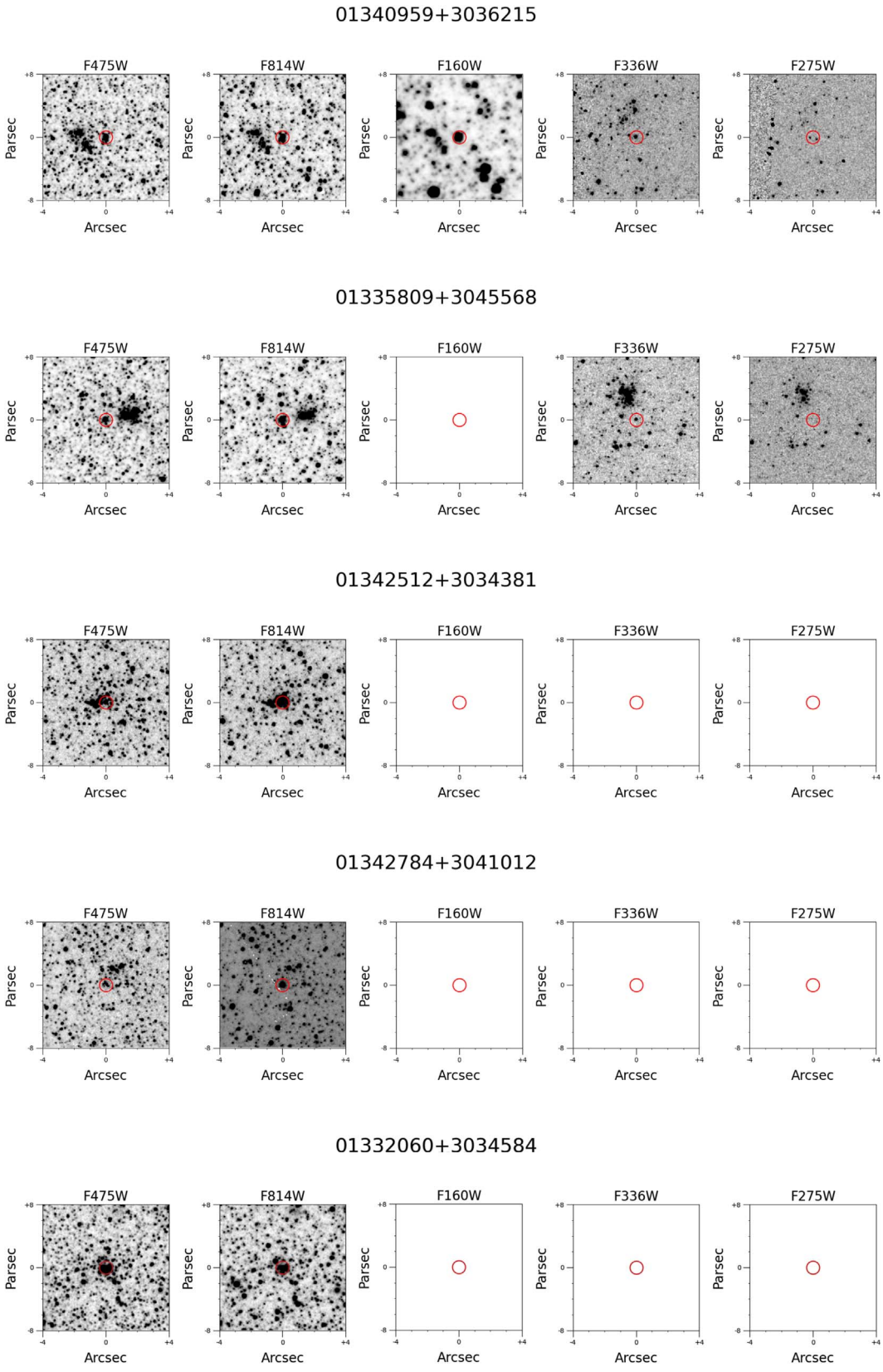

Figure 11. (Continued.)

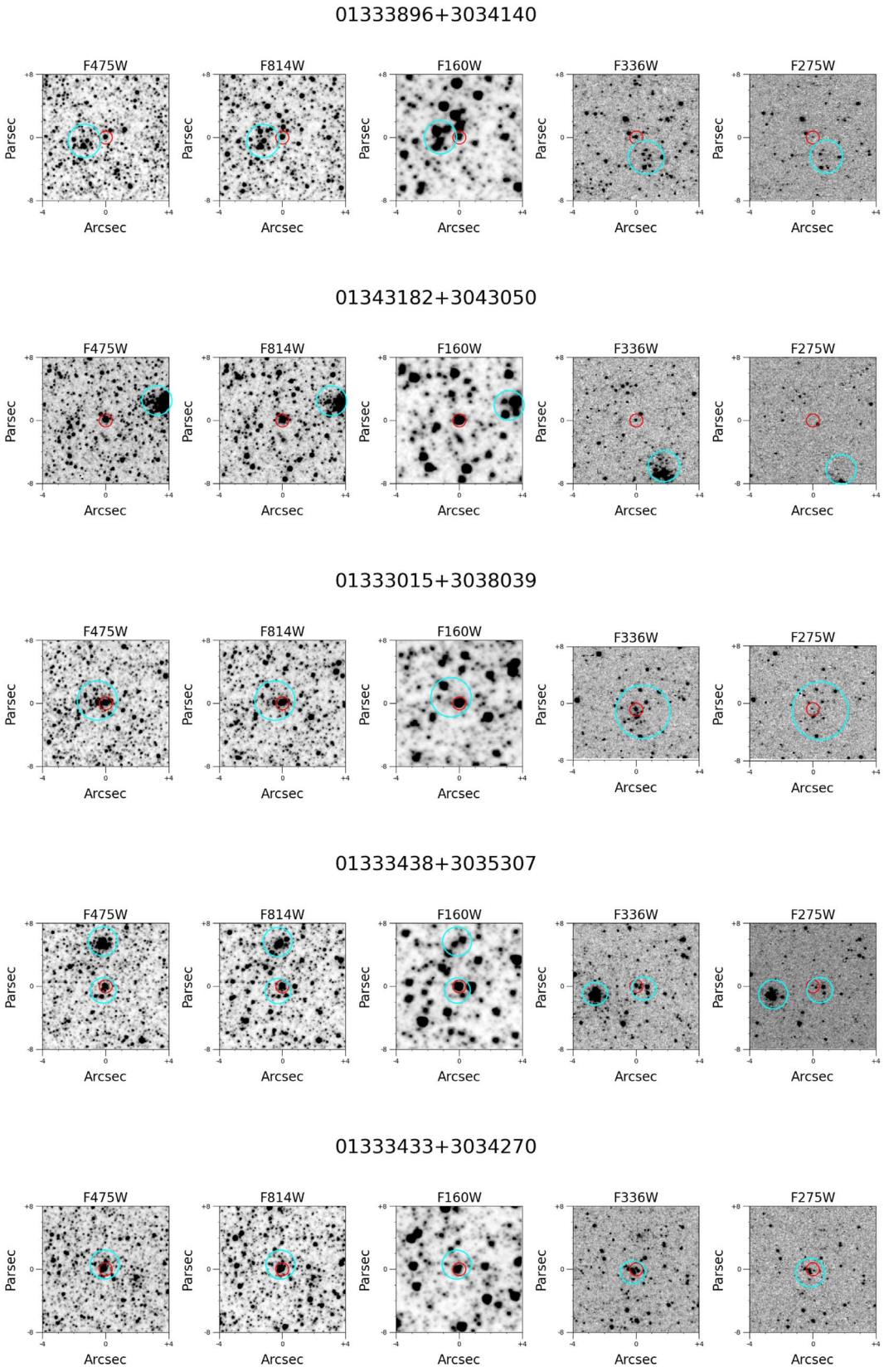

Figure 12. Postage stamps in HST filters for the 13 additional cluster Cepheids found by visual inspection. The position of suspected clusters is shown in blue.

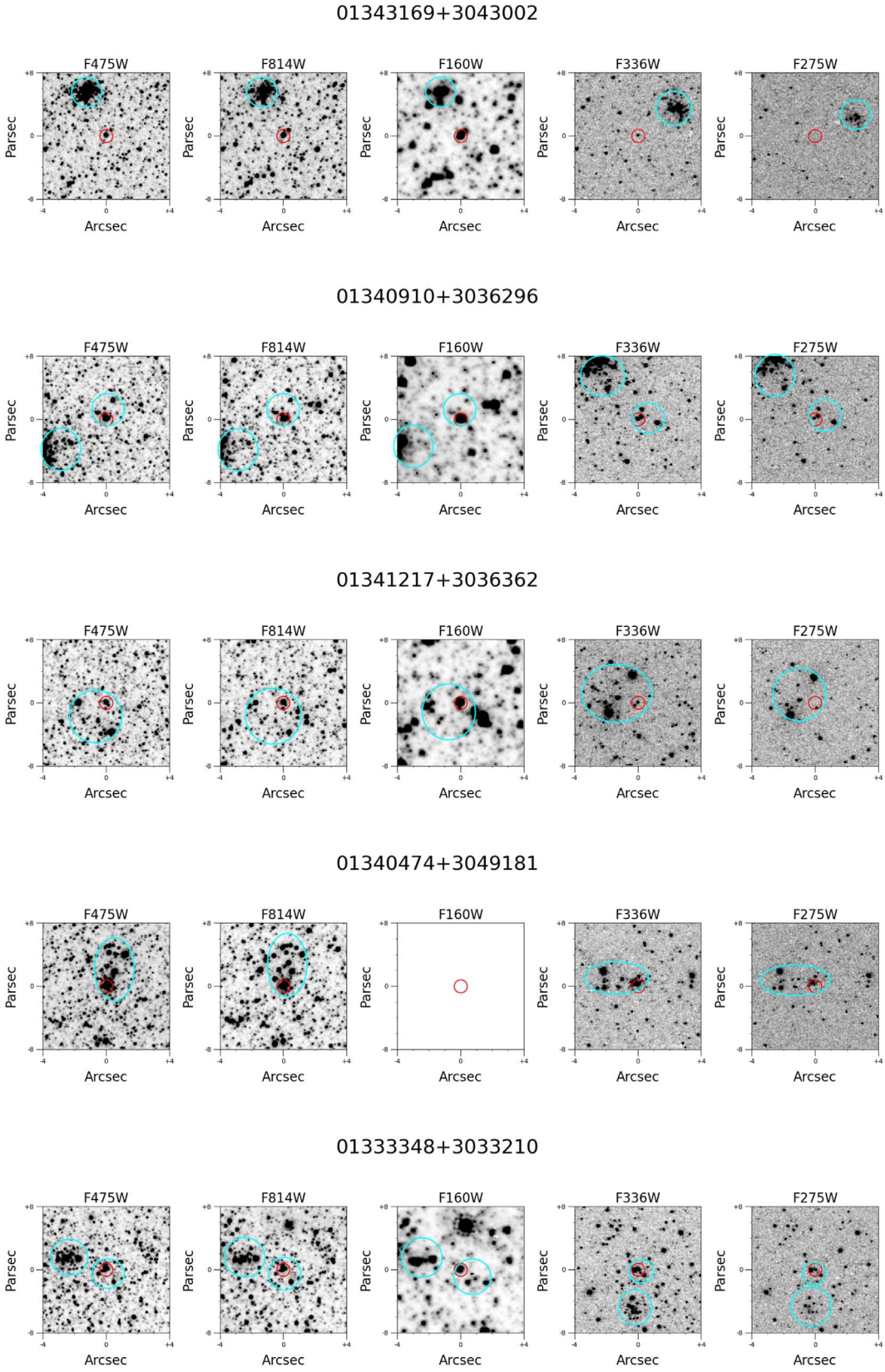

Figure 12. (Continued.)

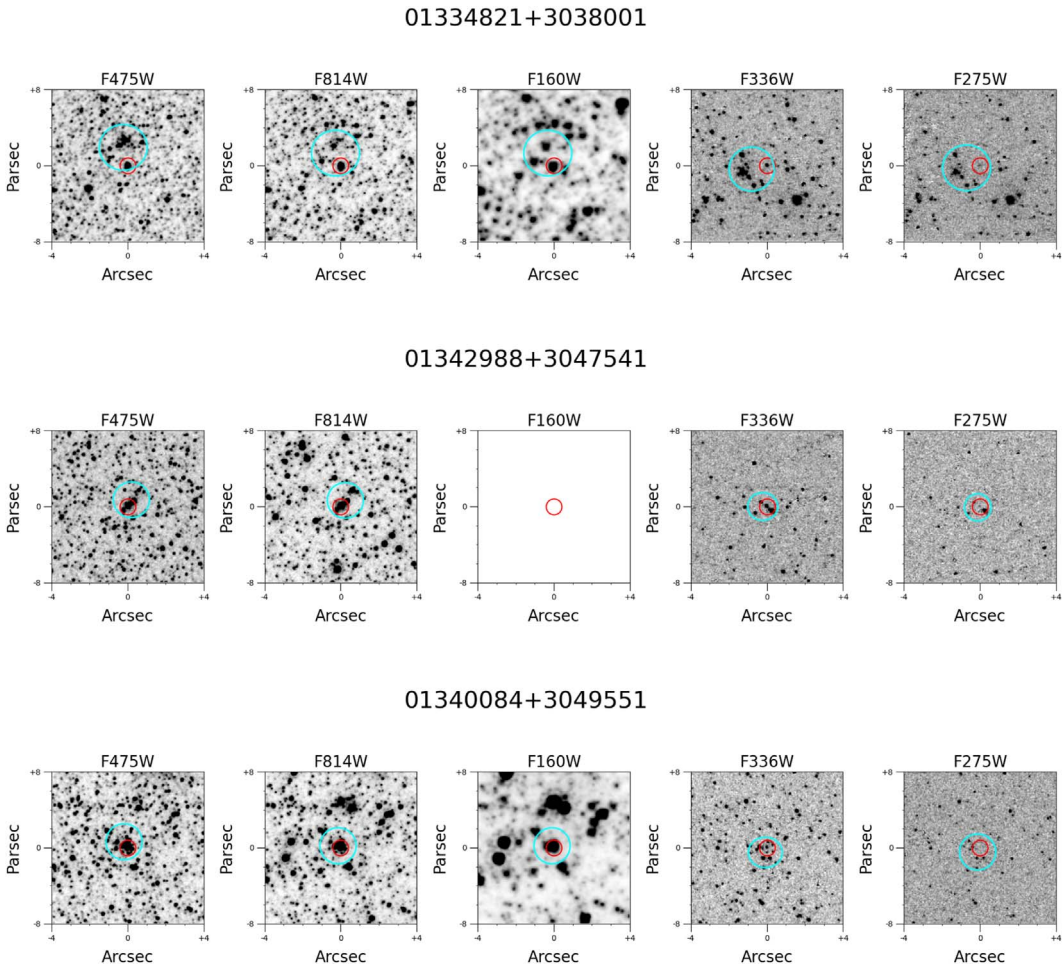

Figure 12. (Continued.)

ORCID iDs

Louise Breuval https://orcid.org/0000-0003-3889-7709
Adam G. Riess https://orcid.org/0000-0002-6124-1196
Lucas M. Macri https://orcid.org/0000-0002-1775-4859
Siyang Li https://orcid.org/0000-0002-8623-1082
Wenlong Yuan https://orcid.org/0000-0001-9420-6525
Tarini Konchady https://orcid.org/0000-0003-0452-9182
Boris Trahin https://orcid.org/0000-0001-5875-5340
Meredith J. Durbin https://orcid.org/0000-0001-7531-9815
Benjamin F. Williams https://orcid.org/0000-0002-7502-0597

References

Anderson, R. I., Koblischke, N. W., & Eyer, L. 2023, arXiv:2303.04790
Anderson, R. I., & Riess, A. G. 2018, ApJ, 861, 36
Antonello, E., Fugazza, D., & Mantegazza, L. 2000, A&A, 356, L37
Asplund, M., Grevesse, N., Sauval, A. J., & Scott, P. 2009, ARA&A, 47, 481
Astropy Collaboration, Price-Whelan, A. M., & Sipőcz, B. M. 2018, AJ, 156, 123
Bhardwaj, A., Kanbur, S. M., Macri, L. M., et al. 2016, AJ, 151, 88
Bonanos, A. Z., Stanek, K. Z., Kudritzki, R. P., et al. 2006, ApJ, 652, 313
Bresolin, F. 2011, ApJ, 730, 129
Bressan, A., Marigo, P., Girardi, L., et al. 2012, MNRAS, 427, 127
Breuval, L., Kervella, P., Wielgórski, P., et al. 2021, ApJ, 913, 38
Breuval, L., Riess, A. G., Kervella, P., Anderson, R. I., & Romaniello, M. 2022, ApJ, 939, 89
Chambers, K. C., Magnier, E. A., Metcalfe, N., et al. 2016, arXiv:1612.05560
Conn, A. R., Ibata, R. A., Lewis, G. F., et al. 2012, ApJ, 758, 11
Durbin, M. J., Beaton, R. L., Dalcanton, J. J., Williams, B. F., & Boyer, M. L. 2020, ApJ, 898, 57
Fitzpatrick, E. L. 1999, PASP, 111, 63
Freedman, W. L., Madore, B. F., Gibson, B. K., et al. 2001, ApJ, 553, 47
Freedman, W. L., Wilson, C. D., & Madore, B. F. 1991, ApJ, 372, 455
Gieren, W., Górski, M., Pietrzyński, G., et al. 2013, ApJ, 773, 69
Graczyk, D., Pietrzyński, G., Thompson, I. B., et al. 2020, ApJ, 904, 13
Hartman, J. D., Bersier, D., Stanek, K. Z., et al. 2006, MNRAS, 371, 1405
Hertzsprung, E. 1926, BAN, 3, 115
Hoyt, T. J. 2023, NatAs, 7, 590
Hubble, E. P. 1926, ApJ, 63, 236
Inno, L., Matsunaga, N., Romaniello, M., et al. 2015, A&A, 576, A30
Jang, I. S., & Lee, M. G. 2017, ApJ, 835, 28
Johnson, L. C., Wainer, T. M., Torresvillanueva, E. E., et al. 2022, ApJ, 938, 81
Kodric, M., Riffeser, A., Seitz, S., et al. 2018, ApJ, 864, 59
Kourkchi, E., Tully, R. B., Eftekharzadeh, S., et al. 2020, ApJ, 902, 145
Leavitt, H. S., & Pickering, E. C. 1912, HarCi, 173, 1
Lee, A. J., Rousseau-Nepton, L., Freedman, W. L., et al. 2022, ApJ, 933, 201
Li, S., Riess, A. G., Busch, M. P., et al. 2021, ApJ, 920, 84
Macri, L. M. 2001, PhD thesis, Harvard Univ.
Macri, L. M., Stanek, K. Z., Sasselov, D. D., Krockenberger, M., & Kaluzny, J. 2001, AJ, 121, 870
Magrini, L., Stanghellini, L., & Villaver, E. 2009, ApJ, 696, 729
Massey, P., Olsen, K. A. G., Hodge, P. W., et al. 2006, AJ, 131, 2478
McConnachie, A. W., Irwin, M. J., Ferguson, A. M. N., et al. 2004, MNRAS, 350, 243
McConnachie, A. W., Irwin, M. J., Ferguson, A. M. N., et al. 2005, MNRAS, 356, 979
Monson, A. J., Freedman, W. L., Madore, B. F., et al. 2012, ApJ, 759, 146
Ou, J.-Y., Ngeow, C.-C., Bhardwaj, A., et al. 2023, AJ, 165, 137

Pellerin, A., & Macri, L. M. 2011, ApJS, 193, 26
Pietrzyński, G., Graczyk, D., Gallenne, A., et al. 2019, Natur, 567, 200
Press, W. H., Teukolsky, S. A., Vetterling, W. T., & Flannery, B. P. 1992, Numerical Recipes in FORTRAN. The Art of Scientific Computing (Cambridge: Cambridge Univ. Press)
Reid, M. J., Pesce, D. W., & Riess, A. G. 2019, ApJL, 886, L27
Riess, A. G., Casertano, S., Yuan, W., et al. 2021, ApJL, 908, L6
Riess, A. G., Casertano, S., Yuan, W., Macri, L. M., & Scolnic, D. 2019a, ApJ, 876, 85
Riess, A. G., Fliri, J., & Valls-Gabaud, D. 2012, ApJ, 745, 156
Riess, A. G., Macri, L., Casertano, S., et al. 2009, ApJ, 699, 539
Riess, A. G., Narayan, G., & Calamida, A. 2019b, Calibration of the WFC3-IR Count-rate Nonlinearity, Sub-percent Accuracy for a Factor of a Million in Flux, Instrument Science Report WFC3 2019-01, Space Telescope Science Institute
Riess, A. G., Yuan, W., Macri, L. M., et al. 2022, ApJL, 934, L7
Rizzi, L., Tully, R. B., Makarov, D., et al. 2007, ApJ, 661, 815
Rogers, N. S. J., Skillman, E. D., Pogge, R. W., et al. 2022, ApJ, 939, 44
Romaniello, M., Riess, A., Mancino, S., et al. 2022, A&A, 658, A29
Sarajedini, A., Barker, M. K., Geisler, D., Harding, P., & Schommer, R. 2006, AJ, 132, 1361
Sarajedini, A., & Mancone, C. L. 2007, AJ, 134, 447
Schlafly, E. F., & Finkbeiner, D. P. 2011, ApJ, 737, 103
Scowcroft, V., Bersier, D., Mould, J. R., & Wood, P. R. 2009, MNRAS, 396, 1287
Senchyna, P., Johnson, L. C., Dalcanton, J. J., et al. 2015, ApJ, 813, 31
Soszyński, I., Gieren, W., & Pietrzyński, G. 2005, PASP, 117, 823
Tiede, G. P., Sarajedini, A., & Barker, M. K. 2004, AJ, 128, 224
Toribio San Cipriano, L., García-Rojas, J., Esteban, C., Bresolin, F., & Peimbert, M. 2016, MNRAS, 458, 1866
U, V., Urbaneja, M. A., Kudritzki, R.-P., et al. 2009, ApJ, 704, 1120
van der Marel, R. P., Fardal, M. A., Sohn, S. T., et al. 2019, ApJ, 872, 24
Wagner-Kaiser, R., Sarajedini, A., Dalcanton, J. J., Williams, B. F., & Dolphin, A. 2015, MNRAS, 451, 724
Williams, B. F., Durbin, M. J., Dalcanton, J. J., et al. 2021, ApJS, 253, 53
Wu, J., Scolnic, D., Riess, A. G., et al. 2022, arXiv:2211.06354
Yoachim, P., McCommas, L. P., Dalcanton, J. J., & Williams, B. F. 2009, AJ, 137, 4697
Yuan, W., Fausnaugh, M. M., Hoffmann, S. L., et al. 2020, ApJ, 902, 26
Yuan, W., Macri, L. M., Javadi, A., Lin, Z., & Huang, J. Z. 2018, AJ, 156, 112
Zgirski, B., Pietrzyński, G., Gieren, W., et al. 2021, ApJ, 916, 19